

## Bubbles generated from wind-steepened breaking waves:

### 1. Bubble plume bubbles

Ira Leifer<sup>1</sup> and Gerrit de Leeuw<sup>2</sup>

Received 19 August 2004; revised 23 August 2005; accepted 30 September 2005; published 16 June 2006.

[1] Measurements of bubble plumes from paddle-amplified, wind stress breaking waves were made in a large wind-wave channel during the LUMINY experiment in fresh (but not clean) water. Bubble plumes exhibited considerable variability with respect to dynamics, bubble size distribution, and physical extent. A classification scheme was developed, and time- and size-resolved bubble population distributions were calculated for each plume class. Comparison of the bubble distributions suggested that there were two primary types of bubble plumes, termed dense and diffuse on the basis of the ability to optically obscure the background. Diffuse plumes at injection were weakly size-dependent to 1000- $\mu\text{m}$  radius, with a steep decrease for larger bubbles. Dense plumes were multimodal with a steep decrease for small bubbles, a second peak at 1700–2000- $\mu\text{m}$  radius, and a steep decrease for larger bubbles. Because of this peak, large bubbles contributed to total plume bubble volume much more significantly for dense plumes than diffuse plumes. Void fractions of diffuse plumes were greater at maximum penetration than for dense plumes. Finally, the injection and rise phases were approximately equal in time.

**Citation:** Leifer, I., and G. de Leeuw (2006), Bubbles generated from wind-steepened breaking waves: 1. Bubble plume bubbles, *J. Geophys. Res.*, *111*, C06020, doi:10.1029/2004JC002673.

#### 1. Introduction

[2] Bubbles formed by breaking waves are either dominant, or very important to many geophysical processes as diverse as air-sea gas transfer [Liss *et al.*, 1997], aerosol formation [Monahan, 1986], surface microlayer enrichment [Blanchard, 1989], and turbulence generation [Thorpe, 1982]. Each of these processes is potentially important on both regional and global scales. When a wave breaks, it forms bubbles in a bubble plume spanning a wide range of bubble sizes, intense turbulence, and fluid motions. The majority of the larger bubbles rapidly return to the surface; however, many (primarily smaller) bubbles either remain behind or diffuse out of the bubble plume, forming a quasi steady state, background bubble population. In ocean sonar data this appears as a more or less continuous strata of bubbles near the sea surface with “billowy” plumes for stable or “tendrill-like” plumes for unstable atmospheric conditions [Thorpe, 1986]. The plume and background distributions are very different and require separate consideration when assessing the importance of bubble-mediated processes.

[3] The bubble size distribution in the bubble plume is weakly size-dependent and spans a wide size range from tens of micrometers to very large bubbles ( $\sim 1\text{-cm}$  diameter)

[Haines and Johnson, 1995]. Also, they are more spatially homogeneous [Haines and Johnson, 1995] than the background population. While the background population decreases exponentially with depth [e.g., Wu, 1979], some observations suggest the plume population does not. Bubble plumes are both spatially local and transient [e.g., Crawford and Farmer, 1987] on short time and distance scales. In contrast, the background population varies on much larger time and horizontal spatial scales, thus over the size and timescales of a bubble plume, the background distribution can be considered horizontally homogeneous and steady state. For conditions where bubble plumes are largely discrete (i.e., nonoverlapping) bubble plume lifetimes are on the order of 1–5 s with spatial dimensions of tens to hundreds of centimeters [Graham *et al.*, 2004]. At very high wind speeds, plume formation occurs more frequently than the plume timescale and closer than the spatial scale, leading to considerable plume overlapping. From field sonar observations [Crawford and Farmer, 1987], overlapping can be significant for small bubbles for wind speeds as low as  $11\text{ m s}^{-1}$ .

[4] The most important difference between the background and plume bubble populations is the absence of large bubbles in the background population and their significant presence in the plume population. The background population generally decreases cubically or steeper with radius over a wide size range, from 50  $\mu\text{m}$  to as large as  $\sim 1000\text{ }\mu\text{m}$  radius [Leifer *et al.*, 2006]. Thus large bubbles are relatively rare in the background population. By contrast, bubble size spectra in bubble plumes decrease much more shallowly with equivalent spherical radius,  $r$ . Thus the relative importance of large bubbles is significantly greater (e.g., to plume

<sup>1</sup>Marine Science Institute, University of California, Santa Barbara, California, USA.

<sup>2</sup>TNO Physics and Electronics Laboratory, The Hague, Netherlands.

void fraction). Large bubbles are defined as larger than the radius of the onset of oscillations for bubbles rising in quiescent water,  $\sim 700 \mu\text{m}$  at  $20^\circ\text{C}$  [Leifer *et al.*, 2000]. In the lab, Patro *et al.* [2002] observed that large bubbles in seawater acted hydrodynamically clean, that is, uncontaminated, while small bubbles acted hydrodynamically dirty, that is, contaminated. Thus the background population primarily is dominated by contaminated bubbles, while the plume population contains many large and hydrodynamically clean bubbles. Surface contamination is important because dirty bubbles rise slower and exchange gas slower than clean bubbles [Leifer and Patro, 2002]. Another significant difference is that the rise velocity for small bubbles increases strongly with  $r$ , while for large bubbles it is very weakly  $r$  dependant over the range  $800 < r < 5000 \mu\text{m}$  [Leifer and Patro, 2002]. Thus, in the absence of intense turbulence, bubbles smaller than  $r \sim 700 \mu\text{m}$  rapidly size segregate because of buoyant rise [Leifer, 1995], while any size segregation of larger bubbles cannot result from buoyancy. Because of these differences, the two populations can have very different impacts on bubble-mediated geophysical processes.

[5] Most published bubble distributions are of the background population (Leifer *et al.*, submitted manuscript, 2005) with few bubble plume bubble observations for wind-steepened breaking waves (see review, section 3). Moreover, most background bubble measurements are time (and hence spatially) averaged. Certainly, bubble plume bubble measurements present significant challenges. Yet numerical models of many bubble processes, such as air-sea gas exchange, require the bubble source or injection size distribution, rather than the time and spatially averaged background population measurements.

[6] In this paper, we present observations of bubbles in bubble plumes from paddle-steepened wind stress breaking waves during the LUMINY wind wave experiment, hereafter referred to as LUMINY. Bubble plumes exhibited a wide range of variability both spatially and in the bubble size distributions. Many bubble processes (e.g., air-sea gas exchange) are nonlinear with bubble size, bubble depth, plume dimensions, etc. To preserve plume diversity, a classification scheme was developed. Contextual observations from an overview camera were collected simultaneously with bubble plume bubble size distributions allowing interpretation of the bubble spectra with regards to plume characteristics. Also measured were the generation rates for each plume class with regards to fetch, for example, wave development, presented by Leifer *et al.* (submitted manuscript, 2005, hereinafter referred to as LCD). Approximately 3500 plumes were analyzed. Of these, plumes from each class were analyzed, their size distribution as a function of time determined ( $\sim 30$  plumes). The results of this analysis are summarized in this paper.

[7] The classification scheme served several purposes. First, the classification scheme preserved diversity in bubble size distributions between different plume classes. Thus it was discovered that there were two primary categories of plume classes, termed dense and diffuse on the basis of their ability to optically obscure the background. This ability was related to differences in the bubble size distributions.

[8] Second, the classification allowed interpretation of the effects of wave development on bubble plume formation. For example, with increased wave development, the probability of forming dense bubble plumes increased compared to diffuse bubble plumes. When a wave breaks, the energy forms new surface area (bubbles), generates turbulence, and creates bulk fluid motions. We propose that the pathways taken by the wave-breaking energy are related to the generation rates for the different plume classes. Thus the classification scheme allows investigation of the relationship between wave breaking and plume formation.

[9] Finally, by combining the bubble plume bubble size distributions with the generation rates for each plume class, global bubble plume bubble formation rates as a function of fetch were calculated (LCD). These global bubble size distributions were compared with wave development with respect to fetch. Other plume-class characteristics were calculated such as plume bubble formation rate, lifetime, and penetration depth.

## 2. Experiment

### 2.1. LUMINY Wind Wave Study

[10] The objective of the LUMINY study, named after the institute where the experiments took place, was to investigate the relative importance of waves, turbulence, and bubble plumes to air-water gas transfer by studying the transfer rates of different gases for a variety of wind and wave conditions. The LUMINY study was primarily a series of laboratory experiments in the Large Air-Sea Interaction Simulation Tunnel of the Institut de Recherche sur les Phénomènes Hors Equilibre, Laboratoire Interactions Océan-Atmosphère LUMINY (IRPHE-IOA), in Marseille, France. The LUMINY study and first results are described in detail by De Leeuw *et al.* [1999, 2002]. In brief, measurements of air-water gas transfer were made in a 2.5-m-high by 2.6-m-wide by 40-m-long wind-wave channel filled to 0.9 m with filtered and UV-sterilized fresh water. The tank was swept and rinsed before filling but obviously, such a large area could not be really clean. Hence water quality rapidly decreased after filling for the experiments and the water was not clean. Wind speed was varied between  $2 \text{ m s}^{-1}$  and  $13 \text{ m s}^{-1}$ . Wave development could be increased by a paddle wave maker. Paddle waves had a wavelength of 1.3 m, a frequency of 1.2 Hz, and an average height of  $\sim 12 \text{ cm}$  over the fetches surveyed. Bubble plume measurements were for conditions of paddle waves and  $13 \text{ m s}^{-1}$  wind speed. Water temperatures were between  $14^\circ\text{C}$  to  $18^\circ\text{C}$ . Under these conditions, plume overlapping was still negligible at the fetch of peak wave breaking, but rapidly increasing. During these experiments, bubble size distributions as well as breaking-wave characteristics and airflow properties were quantified at various fetches by attaching the instrumentation to a carriage that could be repositioned along the tank [Caulliez, 2002].

[11] Bubbles were observed by two complementary optical bubble measurement systems (BMS) spanning a total range  $10 < r < 5000 \mu\text{m}$ . A  $5 \text{ cm s}^{-1}$  current drove water in the downwind direction. Gases were introduced into the tunnel headspace or into the water through aeration devices. Then, time series of gas concentrations were measured in the water and air to determine the exchange rates. Individual

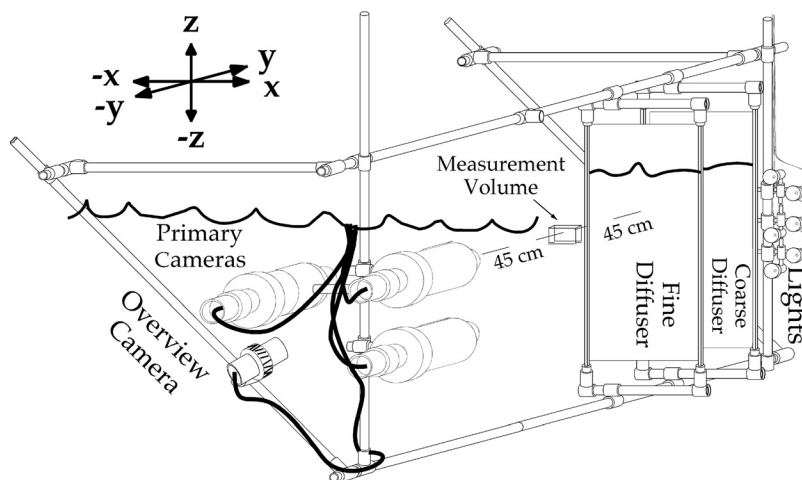


**Figure 1.** National University of Ireland, Galway, bubble measurement system (BMS) schematic.

processes were simulated in an idealized situation to determine the effects on the transfer coefficients of parameters like wave height and slope, bubble generation, wind velocity, and air and water temperatures. Using this data, and theoretical and numerical modeling studies, an improved parameterization of air-sea gas transfer velocities was developed [De Leeuw *et al.*, 1999, 2002; Bowyer and Woolf, 2004].

## 2.2. Bubble Measurement System

[12] The NUIG-BMS was developed for LUMINY at the National University of Ireland, Galway (NUIG) to measure bubbles noninvasively in bubble plumes and near the surface, and to characterize plume dynamics. It is described in detail by Leifer *et al.* [2003b]. Briefly, the NUIG-BMS used multiple video cameras in individual underwater housings to simultaneously observe bubble distributions at multiple resolutions for one or several locations (see Figure 1). Six lights (two per camera) shone on two screens to provide very even back illumination. Components were mounted on a frame that maintained the camera axis perpendicular to the wave direction. The NUIG-BMS made noninvasive measurements of bubble plumes near the interface thanks to its unconstrained and distant measurement volume. An overview camera with a wide field of view observed the measurement volume, albeit from a different angle, and ensured that bubbles produced by the housings were not advected near the measurement volume. The overview camera also provided contextual observations of plume structure and dynamics. Besides aiding interpretation of bubble plume size distributions (particularly for large plumes), this information was used to determine the generation rates for different plume classes at different fetches (see LCD). The NUIG-BMS effectively observed bubbles from  $r = 150 \mu\text{m}$  to the largest bubble observed,  $r \sim 7000 \mu\text{m}$ .

## 2.3. Bubble Analysis

[13] The analysis methodology is presented by Leifer *et al.* [2003b]. In brief, bubble size was determined by discriminating bubbles from the background through image thresholding of in-focus bubbles. Routines were written in NIH Image (NIH Image Software, NIH Image version 1.62b30, developed at the U.S. National Institutes of Health,

available at <http://rsb.info.nih.gov/nih-image/>). Where possible, bubbles were manually tracked between frames, allowing identification of partially or completely obscured bubbles. Typically, the outlines of obscured bubbles were identified through the frontward bubble, aided by routines that predicted the bubbles' location in the subsequent frame. Small bubbles often were blurred because of motion and were sized at or near maximum penetration when they were nearly motionless. Additionally, some bubbles were blurry because of being at the edge of the in-focus region. These bubbles were sized when in focus, or were not counted. Because of the high void fraction, which caused touching and overlapping bubbles, and the irregular shape of large bubbles, manual bubble analysis often is required within bubble plumes [Haines and Johnson, 1995]. Additionally, cameras were aimed slight upward ( $\sim 10^\circ$ ) to minimize wave trough interference for the highly three-dimensional waves. This caused part of the image to have a "textured" background. Where necessary (i.e., in most cases), bubbles were manually outlined, and a best fit ellipse calculated (major and minor axes and angle) with a least squares, linear regression analysis. From the two axes, the equivalent spherical radius,  $r$ , was calculated. Then, the bubble size distribution was calculated by histogramming the time series of  $r$  using routines written in Matlab (Mathworks, MA). Size distributions were calculated by histogramming for each time interval with logarithmically spaced radius bins, spanning  $100 \mu\text{m} < r < 5000 \mu\text{m}$ , and were normalized to units of  $\mu\text{m}^{-1}$ .

[14] Bubble size distributions generally are described by a power law dependency [e.g., Johnson and Cooke, 1979],

$$F(r, t) = k r^{-S(t)} \quad (1)$$

where  $S$  is the power law exponent and varies with time,  $t$ ,  $k$  is a constant, and  $F$  is the bubble size distribution (concentration or population).  $S$  was calculated by a least squares, linear regression analysis of the log of both sides of (1) over an appropriate  $r$  range. Typically, bubble size distributions are reported as concentration size distributions,  $\phi$  ( $\mu\text{m}^{-1} \text{cm}^{-3}$ ) [e.g., Medwin and Breitz, 1989]. However, bubble plumes from breaking waves are discrete and

transient, thus the population size distribution,  $\Phi$  ( $\mu\text{m}^{-1}$ ) is a more meaningful quantity because it is approximately conserved during injection until maximum penetration, when the plume achieves its deepest extent and the bubbles are at their injection depth. The population distribution only decreases as bubbles begin surfacing (dissolution can be neglected during the 0.5 to 1.5 s plume lifetimes for bubbles in the size range of the NUIG BMS).  $\Phi$  is the total number of bubbles in the plume per unit radius ( $\mu\text{m}$ ). In contrast,  $\phi$  decreases with time because of plume growth, thus for modeling purposes, interpretation of  $\phi$  requires the time-varying plume dimensions.

#### 2.4. Scaling to Plume Population

[15] Shallow plumes for analysis were chosen which had all their bubbles in the wide camera's field of view (FOV) and were in focus; that is, they were within the depth of field (DOF). For the narrow FOV camera and for deep plumes, only a portion of the plume was imaged, thus  $\Phi$  for the FOV was scaled to the plume  $\Phi$ . This scaling factor relates plume size to camera FOV and DOF and assumes plume homogeneity. Plume size was estimated at maximum penetration from overview camera images by measuring the vertical and horizontal extents and shape, and assuming horizontal dimensions were symmetric. Plume horizontal dimensions were assumed radially symmetric. Discrimination between the deep and shallow classes was based on whether the penetration depth,  $z_B$  was greater or less than 15 cm, that is, a depth comparable to the typical height of the breaking waves (LCD).

[16] Plume homogeneity is an important assumption for accurate scaling to the plume population. For shallow plumes, there was size segregation with depth, but because the entire plume was in the field of view, scaling was unnecessary. For larger plumes, the validity of this assumption rests on how well mixed they were. The very largest plumes observed were well mixed, and showed excellent agreement between the narrow and wide FOV cameras [Leifer and De Leeuw, 2002]. Smaller plumes showed poorer agreement between the wide and narrow FOV cameras, which was attributed to spatial heterogeneity. In bubble plume bubbles from a tipping bucket, Haines and Johnson [1995] did not observe an exponential decrease in  $\phi$  with depth (i.e., the spatial distribution of bubbles was homogeneous within the plume). The authors attributed this to the influence of the tank bottom on the bubble plume.

[17] The assumption of horizontal heterogeneity could not be verified with this data set as an additional upward looking camera would have been required. Thus plumes could have been elongated in the downstream direction, which would have introduced a bias toward overestimating plume volume (and thus lower void fraction). As a result, values of plume volume must be considered approximate. However, the bubble trajectories at maximum penetration suggest that any such bias would have been small. During injection, plume motions were largely linear; but this changed into large eddy-like motions at maximum penetration, which were highly three dimensional.

#### 2.5. Calibration

[18] To minimize interference with bubble plume development and to prevent bubble generation by the BMS, the

NUIG-BMS was designed to be noninvasive, that is, a distant and unconstrained measurement volume. However, the noninvasive design increased the difficulty of calibration; that is, how efficiently did the camera observe and size bubbles in its FOV and DOF? One calibration approach was to compare the size distributions of a well-mixed plume observed simultaneously by both the wide and narrow FOV cameras, scaling for the different FOVs and DOFs. Agreement between the two was excellent for bubbles with a diameter larger than 5 pixels [Leifer and De Leeuw, 2002], the effective minimum resolution radius. For the wide FOV camera this was equivalent to  $r > 250 \mu\text{m}$ . Although the NUIG-BMS observed bubbles smaller than 5 pixels, various factors decreased the probability of identification including bubble blurring from motion, water turbidity, location at the edge of the DOF, and reduced contrast. Thus measurements of these smaller bubbles became less and less reliable with decreasing size.

[19] Another calibration approach was to compare the NUIG-BMS with the TNO-BMS, which had a constrained measurement volume and is described in Leifer *et al.* [2003b]. Intercomparison between  $\phi$  for bubbles from a porous ceramic aeration device demonstrated good agreement for bubbles over the overlapping size range [Leifer *et al.*, 2003b].

[20] Because of the requirement for the wide FOV camera to image entire bubble plumes, the f-stop was set as high as illumination allowed, F5.6 to F8, resulting in a DOF of  $\sim 4$  cm. The downside of a large DOF is an increased uncertainty in bubble size because of a greater uncertainty in its distance from the camera. This effect was minimized by using longer-focal length lenses. For the wide FOV lens, parallax uncertainty for the wide FOV camera was  $\sim 2.6\%$ ; for the narrow FOV camera, it was about a quarter, that is, 0.7%. Thus, for these long-focal length lenses, the size scale error was negligible (less than 1 pixel) for even the largest bubbles. For small bubbles, the finite dimension represented by individual pixels creates a greater uncertainty. Furthermore, the primary effect of parallax is to broaden peaks in the calculated bubble size distributions, it does not result in a radius shift of a peak.

[21] Measured bubble size varies with the image threshold level, yet most published optical bubble measurements do not report their thresholding methodology. A series of calibration experiments were conducted where optical size was compared with displaced-mass volumetric measurements. Results agreed well with a geometric model, which showed that for back-lit bubbles, the appropriate threshold level is *slightly below* the background intensity [Leifer *et al.*, 2003a]. This results from off-axis reflection from the bubble's front face of light from the backlighting illumination screen. This reflection obscures the bubble's edge. Using the equations of Leifer *et al.* [2003a] and the appropriate parameters for the wide FOV camera, bubble edge obscuration for a  $r = 1000\text{-}\mu\text{m}$  bubble thresholded at the background intensity was 0.5% to 2% depending upon where the bubble was in the FOV. The bias is even less for the narrow FOV camera. Again, these biases were negligible (less than 1 pixel) and bubbles were thresholded as close to the background as possible. The reason these biases were negligible was due to the long-focal length lenses and long distance to the measurement volume, as dictated by the

**Table 1.** Summary of Published Bubble Plume Observations<sup>a</sup>

Plume Type	$r$ , $\mu\text{m}$	Depth, cm	$S_1$	$R$	$S_2$	BMS	Reference	Comment
Wind wave	60–3000	+10 to –20	2	900	–	Laser	<i>Baldy and Bourgu�el</i> [1987]	Wind
WST	50–5000	18	–	2800	2.7	Photo	<i>Haines and Johnson</i> [1995]	Fresh
WST	250–5000	18	–	600	2.6	Photo	<i>Haines and Johnson</i> [1995]	Salt
WST	50–1100	10–50	2.4	900	–	Laser	<i>Leifer</i> [1995]	Salt
Flume	80–5000	30	1.5	1000	3.3	Video	<i>Deane and Stokes</i> [2002]	Focused wave
Flume	800–4800	0–6	–	–	3.7	Photo	<i>Loewen et al.</i> [1996]	Focused wave
Ocean	160–3000	30	2.2	1500	4.3	Video	<i>Stokes et al.</i> [2002]	
Ocean	250–2700	30	1.8	1000	4.9	Video	<i>Deane and Stokes</i> [2002]	~1 s old

<sup>a</sup> $S$  is the power law exponent closest to formation,  $r$  is radius, and WST is white cap simulation tank.  $S_1$  is for  $r < R_1$ ,  $S_2$  for  $r > R_1$ , and  $R_1$  is a critical radius in the size distribution.

NUIG-BMS’s noninvasive design. However, for BMSs with shorter–focal length lenses, and with measurement volumes near the camera, these uncertainties can be significant.

[22] To achieve sufficient lighting for an f-stop of f5.6 to f8 required a shutter speed of  $\sim 1/500$  s. As a result, bubble motion caused blurring for bubbles moving faster than one pixel in  $1/500$  s. A calibration experiment investigated the effect of bubble motion blurring on measured bubble size and found it introduced a bias of  $\sim 15\%$  for a  $1000\text{-}\mu\text{m}$  radius bubble moving at  $\sim 30\text{ cm s}^{-1}$  and  $1/500$  s shutter speed [*Leifer et al.*, 2003b]. To minimize this error, blurred bubbles were sized when they reached their injection depth that is, maximum penetration, whenever possible. At maximum penetration, velocities are typically zero to several  $\text{cm s}^{-1}$ , implying a bias error of 1% to 2%. Because smaller bubbles generally were injected faster (which resulted in their predominance in the peripheral regions), often these bubbles blurred significantly during early injection. With regards to this bias during injection, dirty bubbles in the range  $200 < r < 700\text{ }\mu\text{m}$  rise at 4 to  $13\text{ cm s}^{-1}$ , that is, biases of 2 to 7%. However, for this BMS, the bias was less than or equal to the pixel size uncertainty, since these bubbles were 4 to 8 pixels in diameter. A more significant problem is that bubble blurring spreads the bubble image over many pixels, decreasing contrast with the background. As a result, blurred bubbles are less likely to be identified, particularly during the early injection phase or at the edges of the in-focus region. Bubble blurring is one of the factors explaining why the effective minimum resolution is significantly greater than the video pixel resolution [*Leifer et al.*, 2003b].

### 3. Previous Bubble Plume Bubble Measurements

[23] Few bubble measurements exist for bubbles in bubble plumes (summarized in Table 1), even fewer for bubble plumes from wind stress–induced wave breaking. Measurements in Table 1 are those closest to the formation region and time (where measurements were time resolved). In the laboratory, bubble plumes were created by tipping buckets in a whitecap simulation tank (WST), focused wave packets, and wind stress breaking waves. In the laboratory, only *Baldy and Bourgu el* [1987] measured bubbles from wind stress wave breaking near the breaking region. These measurements were at the IRPHE facility, both with and without paddle steepening. Their data showed that while  $S$  was 4 outside the region of active wave breaking,  $S$  decreased to 2 within.

[24] *Haines and Johnson* [1995] reported on photographic, time-resolved WST measurements for bubble plumes in

fresh and salt water. For seawater,  $\Phi$  was flat in the plume center over the range  $300 < r < 1000\text{ }\mu\text{m}$  and roughly flat for fresh water for  $300 < r < 3000\text{ }\mu\text{m}$ . For larger  $r$ ,  $\phi$  decreased with  $S = 2.6$  and  $2.7$  for fresh and salt water, respectively. Thus the primary difference between fresh and salt water was the location of the critical radius in  $\phi$ . Also, *Haines and Johnson* [1995] observed that  $S$  decreased with  $t$  as the plume arrived at 15 cm below the interface; that is, the plume periphery first arrived at their camera location and then the main plume. This explains why their shallowest  $S$  (1.2) occurred 2.3 s after plume formation. Also in a WST, *Leifer* [1995] observed that  $\phi$  steepened with time, increasing from  $S = 2.56$  at 1.2 s after plume formation to  $S = 4$  at 5 s. These distributions were from an integrated, “statistical” three-dimensional plume, measured by repositioning the phase Doppler anemometer (laser) over numerous bucket tips.

[25] For focused-wave wave-breaking bubble plumes, *Deane and Stokes* [2002] reported  $\phi$  decreased with  $S = 1.5$  in the size range  $250 < r < 2700\text{ }\mu\text{m}$  for focused waves, while *Loewen et al.* [1996] used video with a size range that included larger bubbles ( $800 < r < 4800\text{ }\mu\text{m}$ ). They reported a steeper  $\phi$  with  $S = 3.7$ .

[26] *Stokes et al.* [2002] reported  $\phi$  in the open ocean at a depth of 30 cm and moderate wind speeds ( $7\text{--}10\text{ m s}^{-1}$ ). The  $\phi$  showed a critical radius at  $r \sim 700\text{ }\mu\text{m}$  where the distribution steepened from  $S \sim 2.2$  (fit by the authors for data by *Stokes et al.* [2002, Figure 2]) to  $S = 4.3$  for bubbles larger than the critical radius. This was similar to  $S$  for *Loewen et al.* [1996] for  $r > 1500\text{ }\mu\text{m}$ . *Deane and Stokes* [2002] observed  $\phi$  for bubbles in an  $\sim 1$  s old, oceanic bubble plume decrease with  $S = 1.8$ .

## 4. Bubble Plumes

### 4.1. Bubble Plume Classes

[27] Bubble plumes exhibited enormous diversity in spatial extent, energetics, and bubble size distribution. To preserve this diversity, a plume classification scheme was developed. Plumes were classified on the basis of plume horizontal extent,  $w$ , narrow (N) or broad (B), penetration and  $z_p$ , shallow (S) or deep (D), and the plume’s ability to optically obscure (termed dense (De)) or not obscure (termed diffuse (Di)) the background at maximum penetration. Thus the largest plumes were broad, deep, and dense (BDDe). As shown below, the ability of dense plumes to obscure the background was related to a significant population of large bubbles in the plume. A final class, or more accurately subclass of the diffuse plumes were termed micro. Microplumes were the most common plume, the

**Table 2.** Bubble Plume Classification Criteria<sup>a</sup>

Type	Symbol	Criteria
Broad	B	$w > 30$ cm
Narrow	N	$w < 30$ cm
Shallow	S	$z_p < 15$ cm
Deep	D	$z_p > 15$ cm
Dense	De	Background obscured by bubbles for entire injection phase
Diffuse	Di	Background not obscured by bubbles for entire injection phase
Micro		Narrow shallow diffuse, $w < 10$ cm, $z_p < 10$ cm, $N < 100$

<sup>a</sup>Here  $w$  is width,  $z_p$  is penetration depth, and  $N$  is number of bubbles.

smallest in total number of bubbles and extent and lifetime. These classification criteria are summarized in Table 2. Further details, including overview images of each plume type are in (LCD). Upon close inspection, several plume classes (BDDi, NDDi, BSDi, and BSDe) were found to result from the interaction of two plumes formed in close proximity and time. In the following discussion, these interaction plume classes are grouped together.

## 4.2. Bubble Plume Life Stages

[28] We divide the life of wind stress wave-breaking bubble plumes (not plunging-jet bubble plumes such as from focused waves, nor wave breaking due to decreasing water depth, such as at a beach) into four phases: bubble plume formation, injection, rise, and senescence. The plume lifetime,  $\tau$ , comprises the first three phases and where possible was determined from  $\Phi$  and from overview images.  $\tau$  was defined as lasting while  $B_V > e^{-2} B_{VM}$ , where  $B_V$  is the total bubble volume and  $B_{VM}$  is the maximum or peak total bubble volume. Plume lifetimes were calculated either from individual plume  $\Phi$  or from the class average  $\Phi$ .

[29] The bubble plume formation phase lasted 0.1 s or less and includes the initial wave breaking/bubble formation process and subsequent bubble fragmentation. However, bubble coalescence after the period of fragmentation is not considered part of the formation phase. Moreover, bubble coalescence was extremely rare. For example, in one NSDi plume, almost every large bubble bounced at least once with another bubble during injection; but only one case of coalescence was observed. In general, during the rise phase, bubbles were too dispersed to interact.

[30] This paper focuses on the phases subsequent to formation. Images of the injection, rise, and senescence phases are shown in Figure 2 for a narrow shallow dense (NSDe) plume. During injection, bubbles are advected downward. In general, bubble motions during injection were linear with small velocity fluctuations. During the rise phase, bubbles rise toward the surface because of buoyancy. Since the rise velocity increases with  $r$  for  $r < 700$   $\mu\text{m}$ , the larger, faster moving bubbles in this range leave smaller bubbles behind, thereby causing  $\Phi$  to steepen with  $r$ . Also note that during the injection and rise phases (Figures 2a and 2c) most bubbles streak or blur because of motion (1/50 s shutter speed); however, at maximum penetration (Figure 2b), bubbles were nearly stationary and motion blurring was minimal even at this slow shutter speed. Transition to the senescence phase begins at  $\tau$ , after which the plume is composed of the smaller bubbles left behind,

typically with  $r < 200$   $\mu\text{m}$ . Operationally,  $\tau$  is defined as lasting from formation until when the bubble volume has decreased by  $e^{-2}$  from its peak value. During the transition,  $S$  steepens rapidly, while during senescence,  $S$  changes more slowly (the remaining smaller bubbles rise slower). Unlike the rise phase, when the most important advective process is buoyant rise for the larger bubbles in the plume, during senescence, turbulence and wave motions are important, and turbulence causes expansion of the senescence plume.

## 4.3. Diffuse Plumes

[31] Diffuse plumes were the most common plume type in the channel, preferentially occurring in regions of lesser wave development (LCD). For the most part, diffuse plumes were shallow and were most significant with regards to their small bubble contribution. Due in part to their shallowness, the average and the injection distributions for diffuse plumes were similar and their lifetimes were roughly divided equally between the injection and rise phases.

### 4.3.1. Diffuse Bubble Plumes: Microplumes

[32] The most common plumes were microplumes, which were the smallest in extent and total number of bubbles. A wide FOV image of a typical microplume, 0.04 s after formation is shown in Figure 3a. During the initial injection, bubbles descended  $\sim 1$  cm; however, during the following 0.13 s some of the intermediate size bubbles ( $500 < r < 700$   $\mu\text{m}$ ) descended further to the  $z_p$  of  $\sim 5$  cm below the

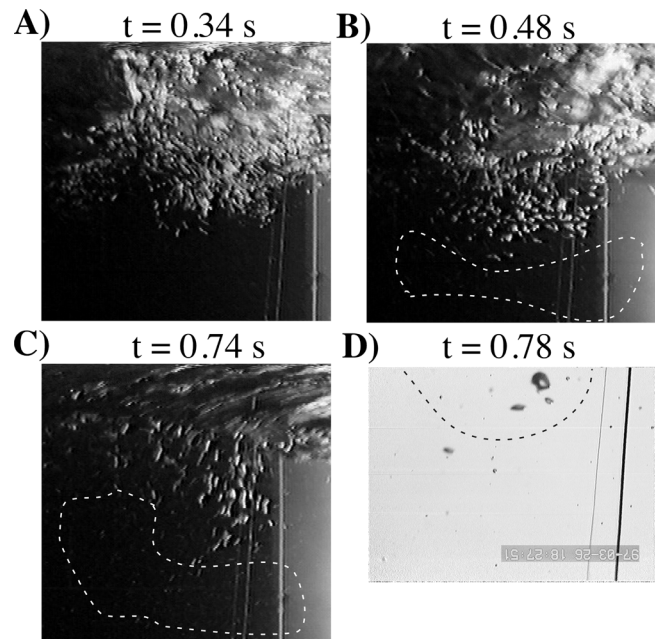


**Figure 2.** Images of the phases of a narrow shallow dense (NSDe) bubble plume for (a) injection, (b) maximum penetration, (c) rise, and (d) senescence phases. Figures 2a–2c were from the overview camera, while Figure 2d was from the narrow field of view camera. Streaks resulted from the 1/50 s shutter speed of the overview camera and the bubble velocity during the injection and rise phases. White dashed line in Figures 2b and 2c outlines plume peripheral region. Black dashed line in Figure 2d outlines the plume during late rise phase; all other bubbles comprise the senescence phase.

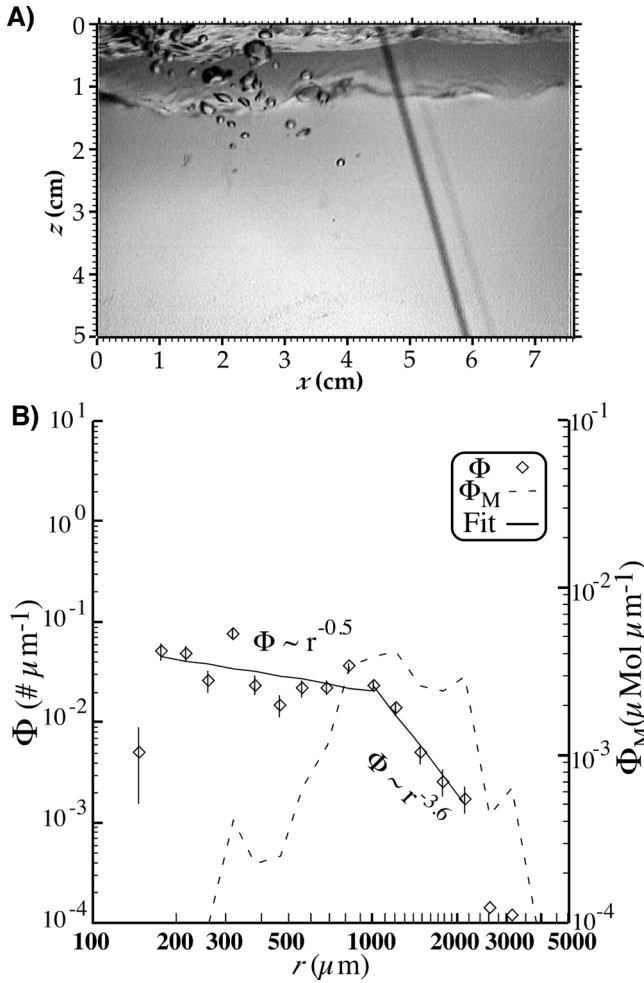


**Figure 3.** (a) Microplume image from the wide FOV camera during injection phase. (b) Population size distribution  $\Phi$ , mass distribution  $\Phi_M$  versus radius  $r$ , and fit to  $\Phi$  over range of  $r$  shown for the plume shown in Figure 3a.

local interface. Because of the small number of bubbles, statistics for individual microplumes were poor.

[33] Microplumes were smaller than the field of view (FOV) and thus did not require scaling. The two size regimes in the individual microplumes were evident in the class injection,  $\Phi_i$ , and lifetime average,  $\Phi_a$ , distributions for the microplume class (Figure 4). For smaller bubbles ( $r < 1000 \mu\text{m}$ ),  $\Phi_i$  decreased shallowly ( $S = 0.4$ ). For larger bubbles ( $r > 1000 \mu\text{m}$ ),  $\Phi_i$  decreased more steeply ( $S = 2.5$ ), but less than cubically, thus the largest bubbles contained most of the plume mass. Because bubbles larger than  $r \sim 7000 \mu\text{m}$  were not observed in microplumes (or any class), the integrated  $\Phi_M$  was finite despite  $S < 3$ . Even though microplumes were the smallest plumes, they occasionally created very large bubbles that survived for a significant fraction of the plume lifetime. Lifetime for the microplume class was 0.4 s, evenly split between the injection and rise phases,  $\sim 0.2$  s. The class-average plume volume,  $P_{VM}$ , at maximum penetration was  $\sim 18 \text{ cm}^3$ . At maximum penetration, the plume bubble volume,  $B_{VM}$ , was  $0.4 \text{ cm}^3$ , thus the void fraction,  $\epsilon$  was  $\sim 2.3\%$ .

**4.3.2. Diffuse Plumes: NSDi**

[34] The next most frequent diffuse plume class was NSDi (LCD). An example image of a NSDi plume during injection is shown in Figure 5a for 0.18 s after (its observed) formation and just before maximum penetration when  $z_P$  was 3 cm. The increase in  $S$  with  $t$  is illustrated in Figure 5b, for  $t = 0.22, 0.36,$  and  $0.48$  s, corresponding to maximum penetration, during the rise phase, and during the transition to senescence, respectively. At maximum penetration ( $t = 0.22$  s)  $\Phi$  increased as  $\Phi \sim r^{+0.4}$  ( $S = -0.4$ ) until a peak at  $r \sim 500\text{--}600 \mu\text{m}$ . For these small bubbles,  $S$  increased with  $t$ , reaching  $S = 1.1$  at the beginning of senescence. Although all NSDi plumes exhibited a decrease in  $S$  with  $t$  after maximum penetration, this plume was exceptional in that initially  $S$  was negative.

[35] This plume’s lifetime average,  $\Phi_a$ , was similar to  $\Phi_a$  for the microplume class with  $S = 0.6$  for small bubbles (not

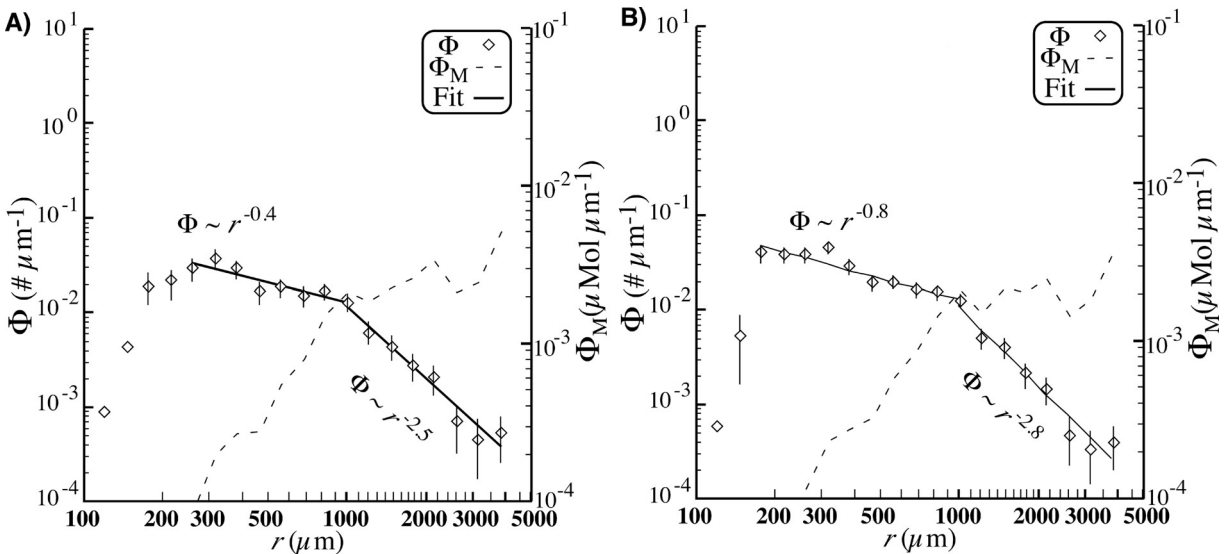


**Figure 4.** (a) Population size distribution  $\Phi$  and mass distribution  $\Phi_M$  for injection for the microplume class versus radius  $r$  and fit to  $\Phi$  and (b) plume life average  $\Phi$  and  $\Phi_M$  distributions versus  $r$  and fit to  $\Phi$ . The  $r$  range of fit shown. Data key is shown in the inset. Error bars are  $\pm 1 \sigma$  (seven plumes analyzed).

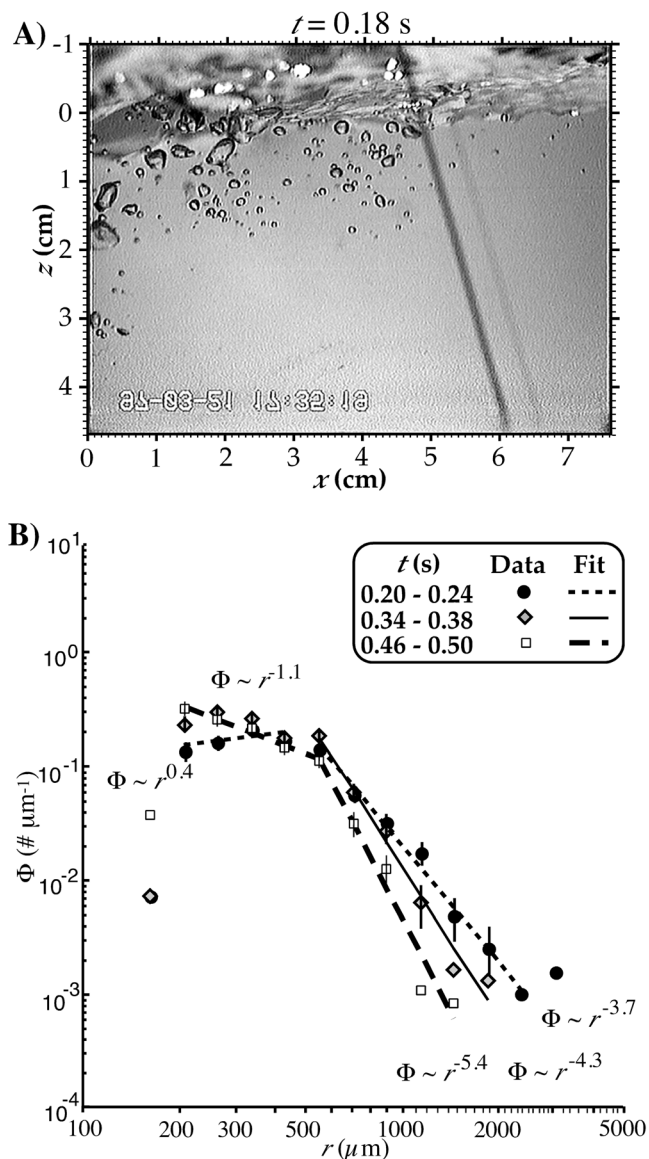


**Figure 5.** (a) Wide FOV image of a minor NSDi plume at time  $t = 0.18$  s and (b) NSDi plume population distributions  $\Phi$  at three different  $t$ . The interface slope in Figure 5a was due to the oncoming subsequent wave crest. Horizontal downwind position  $x$  and depth  $z$  are below the average interface in Figure 5a. Data key and  $r$  range of fits are shown in Figure 5b. Error bars are  $\pm 1 \sigma$ .

shown).  $S$  for larger bubbles ( $r > 600 \mu\text{m}$ ) also increased with  $t$ . The plume image (Figure 5a) clearly shows size segregation with larger bubbles primarily injected to shallower depths than smaller bubbles. At maximum penetration, this plume's bubble volume,  $B_{VM}$ , was  $1.7 \text{ cm}^3$ , while  $P_{VM}$  was  $\sim 200 \text{ cm}^3$  water, or  $\varepsilon \sim 1\%$ . Given that larger bubbles were injected shallower as is apparent in Figure 5a, void fraction was unevenly distributed, decreasing with depth.

[36] The  $t$  and  $r$  variation of  $\Phi$  for the NSDi class is shown in a contour plot (Figure 6a). The injection phase lasted  $\sim 0.2$  s, followed by the rise phase, which lasted

$\sim 0.4$  s. The rise phase is characterized by downward sloping and narrowing contours for larger bubbles. Steeper contours indicate a greater bubble loss rate. The contours narrow with  $t$  during rise as larger bubbles reach the surface sooner than smaller bubbles; that is,  $S$  increased with  $t$  as was seen in Figure 5b. Closed contours at  $t > 0.45$  s are due to the end of the data analysis, which did not continue further into the senescence phase. Although  $\Phi$  for most large bubbles decreased by several orders of magnitude during the rise phase,  $\Phi$  for  $200\text{--}300\text{-}\mu\text{m}$  radius bubbles only decreased by a factor of  $\sim 3$  during the rise phase. Also, some small bubbles were remnants (senescence) from previous plumes.

[37] The NSDi class average  $\Phi$  (Figure 6b) was calculated from  $\Phi(r, t)$  for  $t = -0.16$  to  $0.40$  s. The critical radius,  $R$ , for  $\Phi$  ( $R = 1000 \mu\text{m}$ ) was common to all diffuse plumes and is apparent in the class-average  $\Phi$  where  $S = 1.3$  and  $S = 3.6$  for bubbles with  $r < 1000 \mu\text{m}$  and  $r > 1000 \mu\text{m}$ , respectively. Because  $S > 3$  for  $r > 1000 \mu\text{m}$ , most of the plume mass was contained by bubbles with  $700 < r < 2200 \mu\text{m}$ , with a peak in  $\Phi_M$  at  $r \sim 2000 \mu\text{m}$ . The injection  $\Phi$  for the NSDi class (not shown) was similar to the class-average  $\Phi$  with  $S = 1.0$  and  $S = 3.5$  for bubbles smaller and larger than  $r = 1000 \mu\text{m}$ , respectively. Thus, in terms of several plume characteristics, NSDi plumes were significantly different from microplumes. For NSDi plumes, peak  $B_{VM}$  was  $0.8 \text{ cm}^3$ ,  $z_P$  was  $6 \text{ cm}$ , and at maximum penetration  $P_{VM}$  was  $\sim 120 \text{ cm}^3$ , yielding  $\varepsilon \sim 0.66\%$ .

#### 4.3.3. Diffuse Interaction Plumes: BSDi, NDDi, and BDDi

[38] Three diffuse bubble plume classes resulted from the interaction between two NSDi plumes. These were BDDi, NDDi, and BSDi. BSDi plumes resulted from two NSDi plumes in close proximity (LCD) and had the same distribution as NSDi plumes, with  $\Phi$  roughly twice as large. In general, the two NSDi plumes did not significantly interact, thus  $z_P$  was the same. When they did, they formed the two deep minor plume classes, BDDi and NDDi, which were very rare (LCD). Although these diffuse interaction classes had the same shape injection  $\Phi$  as NSDi plumes, their lifetimes and penetration depths were greater. As a result, the lifetime-average plumes differed significantly from that of the other diffuse plume classes.

[39] An example contour plot of a broad shallow diffuse (BSDi)  $\Phi$  is shown in Figure 7a with the major life phases labeled. These measurements are for the lower periphery of this shallow plume since the camera's FOV was from  $7.4$  to  $13.4 \text{ cm}$  deep. Also, this plume was chosen because it included remnants of a prior NSDi plume formed  $\sim 0.5$  s earlier, which persisted into the BSDi plume. The senescence phase  $\Phi$  ( $-0.5 < t < -0.25$  s) of this remnant NSDi plume is shown in Figure 7b (diamonds). Statistics were poor for the NSDi plume remnants and the best histogram was for just 11 bins spanning the radius range (best is defined by when  $S$  varies the least for a  $\pm 1$  variation in the number of bins). The NSDi senescence  $\Phi$  decreased from the small resolution limit with  $S = 3.4$ . The injection  $\Phi$  for this BSDi plume (Figure 7b, squares) had three regimes, a peak at the lower radius resolution, a weakly  $r$ -dependent "plateau" ( $S = 0.9$ ) extending until  $r \sim 1000 \mu\text{m}$ , and then a sharp decrease for  $r > 1000 \mu\text{m}$  ( $S = 3.1$ ). However, subtraction of the prior NSDi plume's senescence contribution produced an injection  $\Phi$  similar to the NSDi-class  $\Phi$ .

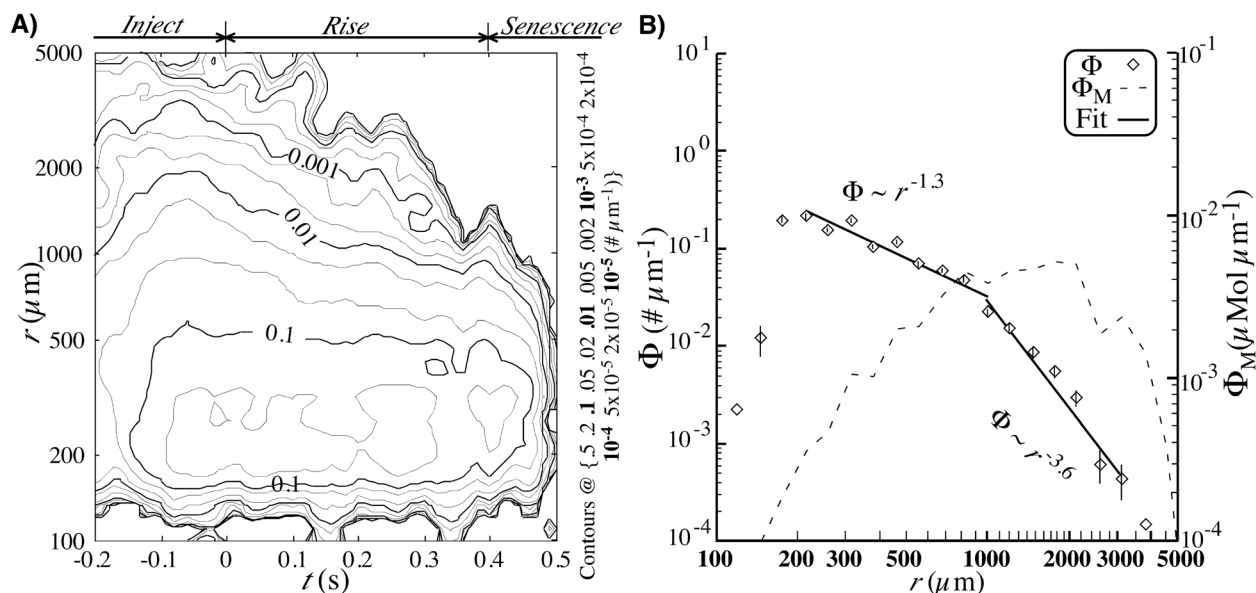


**Figure 6.** (a) Contour plot of the NSDi population distribution  $\Phi(r, t)$ , where  $t$  is time and  $r$  is radius, with  $t = 0$  at maximum penetration.  $\Phi(r, t)$  was cubic spline interpolated to twice the resolution before contouring. (b) Average NSDi-class population size distribution  $\Phi$  and mass distribution  $\Phi_M$  versus  $r$  and fits to  $\Phi$ . Major contours and major life phases are labeled in Figure 6a. Data key and  $r$  range of fit are shown in Figure 6b. Error bars are  $\pm 1 \sigma$  (seven plumes analyzed).

[40] The rarest minor plume class was broad, deep diffuse (BDDi). Overview images showed BDDi plumes resulted from plume-plume interactions at formation in which some bubbles were injected much deeper (see LCD for example). The formation process for NDDi plumes was similar. For all three interaction plumes, the injection  $\Phi$  was twice the NSDi injection  $\Phi$ . While the lifetime and penetration depth for BSDi plumes were the same as for NSDi plumes, both NDDi and BDDi plumes persisted

longer and penetrated deeper. For the latter two,  $z_p$  was  $\sim 18$  cm and  $\tau$  was  $\sim 1.2$  s.

#### 4.4. Dense Plumes

[41] Dense plumes were noticeably distinct from diffuse plumes in several characteristics: their lifetime and distribution, and hence void fraction and bubble volume. Several dense plume classes were deep; however, unlike the deep diffuse plumes, they were not the result of plume-plume

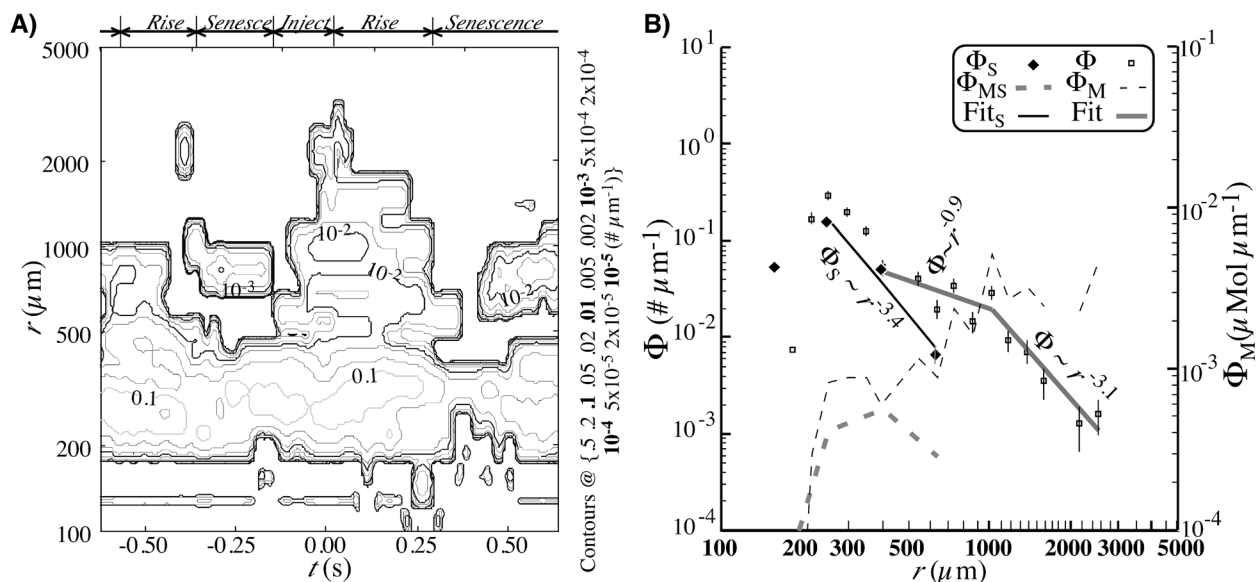


**Figure 7.** (a) Contour plot of BSDi population distribution  $\Phi(r, t)$ , where  $t$  is time and  $r$  is radius, with  $t = 0$  set at maximum penetration, and (b) BSDi injection  $\Phi(r)$  versus  $r$  and fits to  $\Phi$  and mass distributions  $\Phi_M$ . Also shown is  $\Phi_S(r)$  for the remnants of a prior NSDi plume (i.e., senescence phase),  $-0.5 < t < -0.25$  s in Figure 7a. Data key is shown in Figure 7b. Error bars are  $\pm 1 \sigma$ .

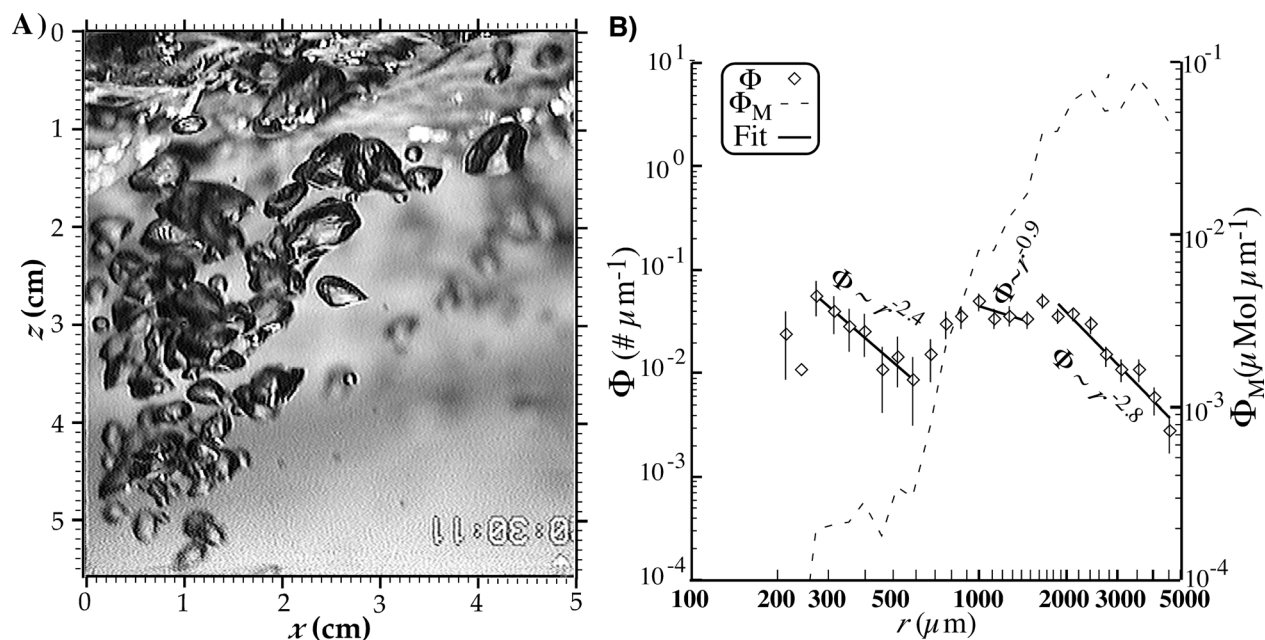


**Figure 8.** (a) Image of NSDe bubble plume and (b) radius  $r$ -dependent injection population distribution  $\Phi(r)$  and mass distribution  $\Phi_M(r)$ , where  $r$  is radius, and fits to  $\Phi$ . Data key is shown in Figure 8b.

interaction. LCD estimated that dense plumes contributed approximately half (56%) of the total bubble volume generation rate in the study area. Thus the significance of these distinct plume classes lies in the nature of their bubble generation. Diffuse plumes primarily injected small bubbles to shallow depths, contributing to the shallow background population. For these shallow plumes, there was little difference between the injection and average distributions. In contrast, dense plumes preferentially generated large bubbles, and many were injected deep. As a result, a significant part of their importance lies in the greater lifetime of these deeper bubbles and their contribution to the deep background population. The most common dense plume class was the narrow shallow dense (NSDe) class. NSDe plumes also exhibited the strongest characteristics of dense plumes. For NSDe plumes, there was little difference between the average and injection distribution. Thus the injection distribution is shown to better compare with the NSDi plumes. For the other dense plume classes, the lifetime average size distributions are presented to demonstrate the importance of the increased plume lifetime.

#### 4.4.1. Dense Plumes: NSDe

[42] An image of a shallow NSDe plume shortly before maximum penetration but still near the interface is shown in Figure 8a. Because of their shallowness and very high bubble concentrations, NSDe plumes were a challenge to image and analyze. For these dense plumes, trajectory analysis was critical to analyzing obscured bubbles. Visual inspection of Figure 8a shows a plume with a paucity of small bubbles and primarily large and very large bubbles. Furthermore, most of the small bubbles were visible at the periphery of the bubble plume. Generally, it was observed that small bubbles were injected significantly faster than larger bubbles and thus tended to be at the plume periphery.

[43] For the NSDe plume in Figure 8a large bubbles were more important to both  $\Phi$  and  $\Phi_M$  (Figure 8b) over the observed size range. The small bubble  $\Phi$  decreased with  $S =$

2.4, until  $r \sim 600 \mu\text{m}$ , when  $\Phi$  increased to a peak at  $r \sim 1000 \mu\text{m}$ . For  $r > 1000 \mu\text{m}$ ,  $\Phi$  was shallow ( $S = 0.9$ ) until  $r \sim 1800 \mu\text{m}$ . A histogram at higher radius resolution (54 radius bins) resolved this peak as statistically significant, although then the statistics for small bubbles were poor [Leifer and De Leeuw, 2002]. For  $r > 2200 \mu\text{m}$ ,  $\Phi$  decreased with  $S = 2.8$ .

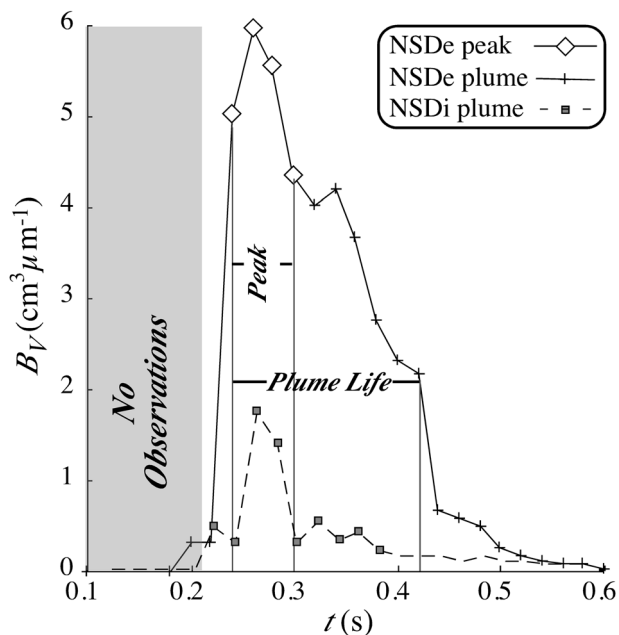


**Figure 9.** (a) Time  $t$  variations in total bubble volume for NSDe plume shown in Figure 8a;  $t$  is after formation. Vertical lines are for the NSDe plume. Time variation in bubble volume for the NSDi plume is for the plume shown in Figure 5a.

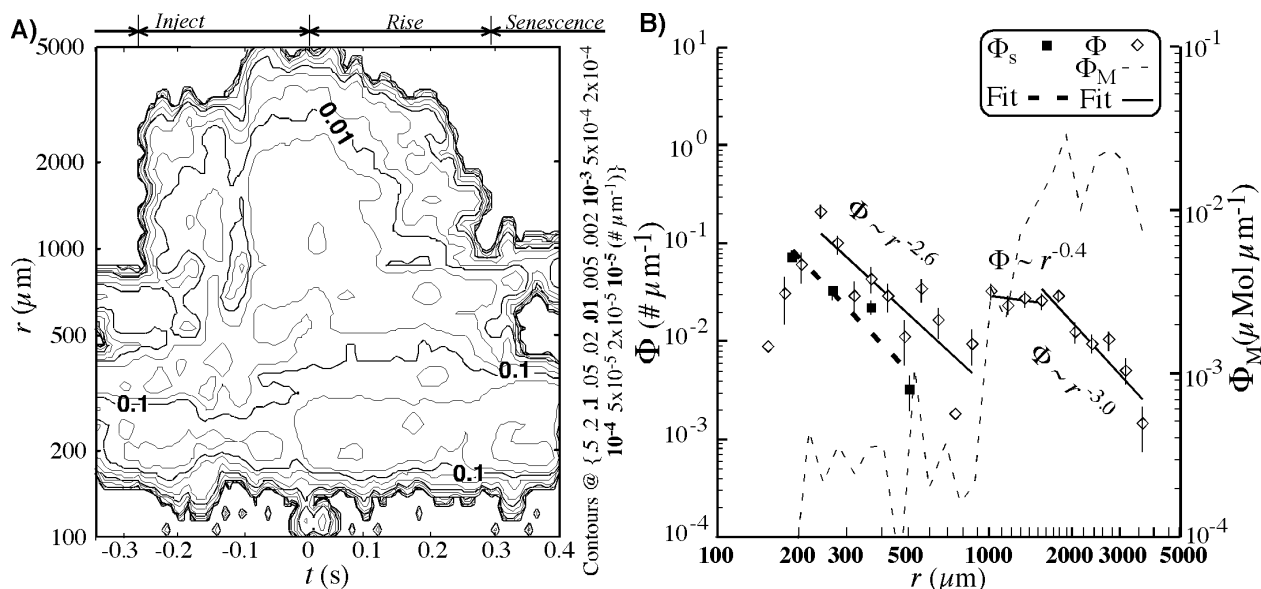


**Figure 10.** (a) Contour plot of the NSDe class distribution  $\Phi(r, t)$ , where  $t$  is time and  $r$  is radius with  $t = 0$  at maximum penetration, and (b) peak NSDe-class  $\Phi$  and mass distributions  $\Phi_M$  with respect to  $r$ . Fits to  $\Phi$  are also shown, as well as preexisting senescence  $\Phi_s$ . Major contours are labeled with contour values in Figure 10a. Data key and  $r$  range of fit are shown in Figure 10b. Error bars are  $\pm 1 \sigma$  (five plumes analyzed).

The peak  $B_V$  for this plume was  $6.0 \text{ cm}^3$  within a volume of  $\sim 300 \text{ cm}^3$  at maximum penetration, yielding  $\varepsilon \sim 2\%$ .

[44] The time-varying  $B_V$  for the NSDe plume shown in Figure 8 is shown in Figure 9. Vertical lines show the averaging times for calculating the peak  $\Phi$  and average plume lifetime  $\Phi$  for this NSDe plume. For the first 0.2 s (injection), the plume was outside the FOV (plume age was determined by comparison with overview images showing the time it took the plume to reach maximum penetration). After maximum penetration,  $B_V$  decreased roughly linearly until  $t \sim 0.44$  s, after which  $B_V$  decreased exponentially during senescence. For comparison,  $B_V(t)$  for the NSDi plume shown in Figure 5a also is shown in Figure 9, with  $t$  shifted so that maximum penetration occurred at the same time as for the NSDe plume. Trends were similar; however,  $B_V$  decreased faster during the rise phase for the NSDi plume. The exponential decrease during senescence phase of the two plumes had similar timescales.

[45]  $\Phi(r, t)$  for the NSDe plume class is shown in Figure 10a and includes preexisting senescence bubbles. The injection and rise phases lasted about the same time,  $\sim 0.25$  s.  $\Phi$  for the injection and preexisting senescence distributions are shown in Figure 10b. For small bubbles,  $S$  for both the NSDe injection and the prior senescence population were similar, with  $S = 2.6$ , and 2.8, respectively. There clearly was an important contribution from senescence bubbles from previous plumes, that is, the background bubble population contribution of small bubbles. Large bubbles were very important to NSDe plumes, for example, bubbles larger than 2000- $\mu\text{m}$  radius contained half the bubble mass. For  $r > 1700 \mu\text{m}$ ,  $\Phi$  decreased rapidly with  $S = 3.0$ .  $B_{VM}$  for the NSDe class was  $3.75 \text{ cm}^3$  in a plume volume of  $P_{VM} \sim 460 \text{ cm}^3$  at maximum penetration,

thus  $\varepsilon \sim 0.81\%$ . Also of note, NSDe plumes persisted longer than NSDi plumes,  $\tau = 0.9$  versus 0.7 s, respectively.

#### 4.4.2. Dense Interaction Plumes: BSDe

[46] There was one dense interaction class, BSDe, which like BSDi plumes, resulted from the interaction between two NSDe plumes formed in close proximity and time. As a result, BSDe and NSDe plumes showed many similarities.

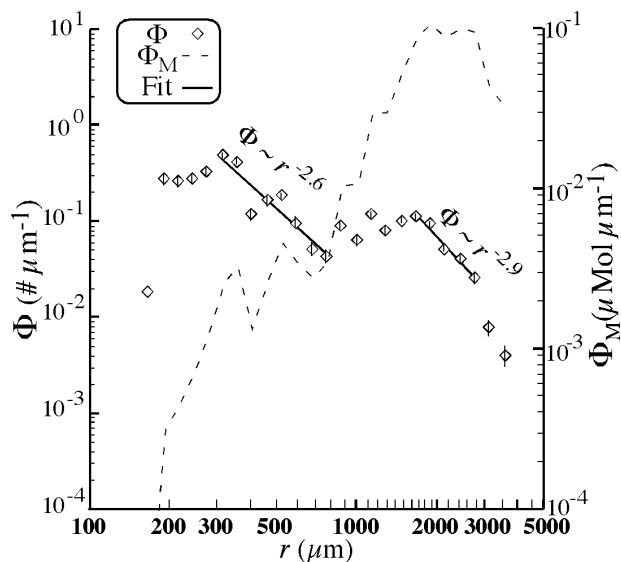


**Figure 11.** Injection BSDe-class population distribution  $\Phi$  and mass distribution  $\Phi_M$  versus radius  $r$  and fits to  $\Phi$ . Note that  $\Phi_M$  is similar to the NSDe-class plume  $\Phi_M$  (Figure 10b). Data key and  $r$  range of fits are shown. Error bars are  $\pm 1 \sigma$  (three plumes analyzed).

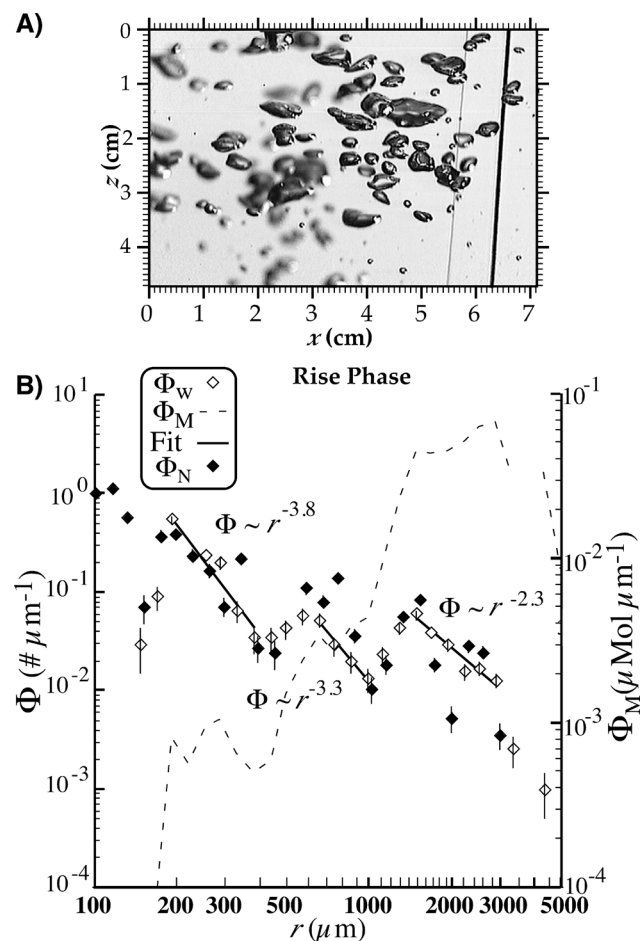


**Figure 12.** (a) Image of a NDDe plume at maximum penetration and (b) rise phase population size distribution  $\Phi$  for wide  $\Phi_W$  and narrow  $\Phi_N$  field of view cameras versus radius  $r$ . Mass distribution  $\Phi_M$  for  $\Phi_W$  and fits for  $\Phi_W$  and  $\Phi_N$  for the NDDe plume are shown in Figure 12a. Horizontal downwind position  $x$  and depth  $z$ , with  $z = 0$  at 7.4 cm below average interface, are shown in Figure 12a. Data key and  $r$  range of fits are shown in Figure 12b. Error bars are  $\pm 1 \sigma$ .

For BSDe plumes, the small bubble  $\Phi$  decreased with  $S = 2.6$  to  $r \sim 700 \mu\text{m}$  and the large bubble  $\Phi$  decreased with  $S = 2.9$  from a peak at  $r \sim 1700 \mu\text{m}$  (Figure 11). Compared to NSDe plumes, the relative contribution of small to large bubbles favored small bubbles for the BSDe class plume. A partial explanation may be that most BSDe plumes were observed at the lower plume periphery. In part this was because interaction plumes were most likely to occur where wave breaking was at a peak; however, to image plumes at the fetch of peak wave breaking the camera was positioned deeper to avoid causing bubbles at the water surface. BSDe plumes had greater  $B_{VM}$  than NSDe plumes,  $4.9 \text{ cm}^3$ , but because of plume-plume interactions, occupied significantly greater volume,  $P_{VM} \sim 2400 \text{ cm}^3$ , yielding  $\varepsilon \sim 0.20\%$ .

#### 4.4.3. Dense Narrow Deep Plumes (NDDe)

[47]  $\Phi$  for a narrow deep dense (NDDe) plumes was similar to NSDe plumes (trimodal with a significant contribution from large bubbles). NDDe plumes had greater  $B_V$  and (by definition) penetrated deeper than NSDe plumes.

However, NDDe plumes occurred about a fifth as often as NSDe plumes (LCD). A wide-FOV camera image of a NDDe plume at maximum penetration is shown in Figure 12a. The top of the FOV was 7.4 cm below the average interface. The  $\Phi$  for the rise phase of the NDDe plume in Figure 12a from the narrow and wide FOV cameras illustrates how measurements near the small resolution limit can be unreliable. For this plume, video was unavailable for injection for the wide FOV camera because of interference from the interface prior to maximum penetration. Video for the narrow FOV camera was available for the injection and rise phases but not at maximum penetration when large bubbles obscured the images.  $\Phi$  from both cameras clearly was trimodal, with peaks at  $r \sim 1600$ ,  $r \sim 650 \mu\text{m}$ , and the small radius measurement limit (Figure 12b). As with other dense plumes, the largest bubbles contained most of the mass. The narrow FOV camera confirmed that the small bubble size distribution included bubbles smaller than  $r \sim 200 \mu\text{m}$ . Moreover, comparison with the narrow FOV camera showed that the steep decrease observed for the wide FOV camera for  $220 < r < 500 \mu\text{m}$  ( $S = 3.8$ ) was due to poorly resolving the small bubble  $\Phi$  in the wide FOV camera. The narrow FOV camera resolved these bubbles better and showed that  $S = 1.6$  for  $120 < r < 400 \mu\text{m}$ . The injection  $\Phi$  (not shown) was similar, but with a steeper  $\Phi$  for small bubbles ( $S = 2.8$ ) and for the intermediate peak ( $S = 1.6$ ), although  $S$  for the largest bubbles was roughly the same ( $S = 2.5$ ). This plume's lifetime was 1.1 s, and had  $B_{VM}$  of  $4.81 \text{ cm}^3$ . At maximum penetration,  $P_{VM} \sim 2000 \text{ cm}^3$ , yielding  $\varepsilon \sim 0.24\%$ .

[48]  $\Phi(r, t)$  for the NDDe class is shown in Figure 13a. NDDe plume lifetime was the longest of all plumes discussed so far ( $\tau = 1.2 \text{ s}$ ), persisting at this depth for 0.7 s. Also, the transition period between injection and rise phases when bubbles were largely neither descending nor rising (maximum penetration) was the longest,  $\sim 0.2 \text{ s}$ .

[49] The lifetime average  $\Phi$  for the NDDe class (Figure 13b) was similar to other dense plumes, specifically the importance (particularly to  $\Phi_M$ ) of large bubbles, with a peak in  $\Phi$  at  $r \sim 1600 \mu\text{m}$ . For  $r > 1600 \mu\text{m}$ ,  $\Phi$  decreased as  $S = 2.9$  until  $r \sim 3000 \mu\text{m}$ , also similar to NSDe plumes, then decreased much more steeply. Steepness of the  $r > 3000 \mu\text{m}$  population most likely resulted from injection segregation; that is, most of the largest bubbles were not injected to the camera depth. There is a suggestion of an intermediate peak at  $r \sim 600 \mu\text{m}$ , but it was poorly resolved. Also,  $\Phi$  was enhanced with regards to small bubbles, similar to observations of the BSDe plumes, although  $S$  for the small bubble  $\Phi$  was less than for NSDe and BSDe plumes with the injection  $S = 2.0$ . The most probable explanation again is size-depth segregation as was apparent in the NDDe plume image shown in Figure 12a, where small bubbles were more common in the deeper (peripheral regions) of the plume. Overall,  $B_V$  for NDDe plumes ( $4.8 \text{ cm}^3$ ) was 28% greater than NSDe plumes, primarily because of the large bubble contribution. At maximum penetration NDDe plumes occupied  $\sim 2400 \text{ cm}^3$ , yielding  $\varepsilon \sim 0.20\%$ .

#### 4.4.4. Dense Plumes: Broad and Deep (BDDe)

[50] Broad deep dense (BDDe) plumes had significantly larger  $B_V$  and dimensions than all other plumes, for example,  $z_p$  was more than 30 cm. BDDe plumes were infrequent, occurring  $\sim 10\%$  as often as NSDe plumes (LCD). They

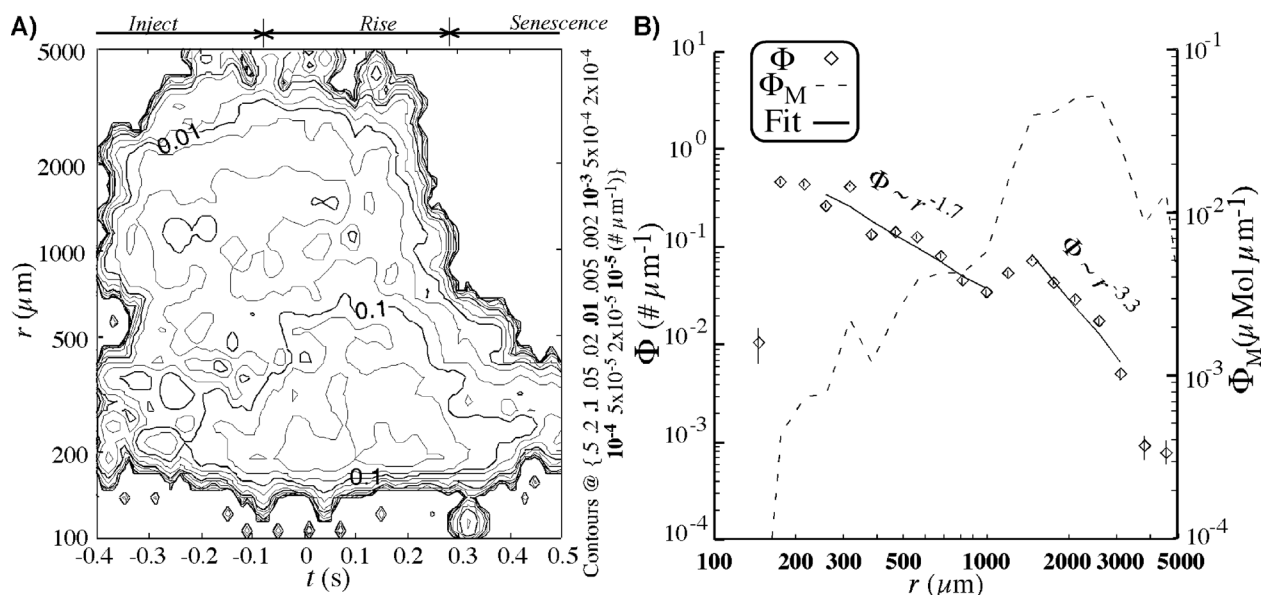


**Figure 13.** (a) Contour plot of time  $t$  and radius  $r$ , varying NDDe-class distribution  $\Phi(r, t)$ , with  $t = 0$  at maximum penetration. (b) Average NDDe-class population distribution  $\Phi$  and mass distribution  $\Phi_M$  versus  $r$  and fits to  $\Phi$ . Major contours (thick lines) are labeled, and contour values are shown in Figure 13a. Data key and  $r$  range of fits are shown in Figure 13b. Error bars are  $\pm 1 \sigma$  (four plumes analyzed).

were also difficult to image for analysis; during several hours of video with the primary cameras only two examples were imaged with sufficient clarity for analysis. Because of their greater turbulence intensity, they were more homogeneous than other plumes, although they exhibited similar size-segregation patterns (smaller bubbles at periphery) as other dense plumes.

[51] Overview camera images of a BDe plume showed that the injection was two phase (Figures 14a and 14b). A

ring of bubbles initially descended while expanding rapidly in diameter, and then quickly decelerated (Figure 14b). A few tens of milliseconds later, a jet of bubbles descended through the center of the bubble ring (Figure 14a overtaking the ring (Figure 14b) and continued descending and expanding until maximum penetration at  $\sim 0.7$  s shown in Figure 14c; see LCD for overview image at maximum penetration). BDe plumes were significantly larger than the FOV and broader than the DOF, requiring plume scaling.

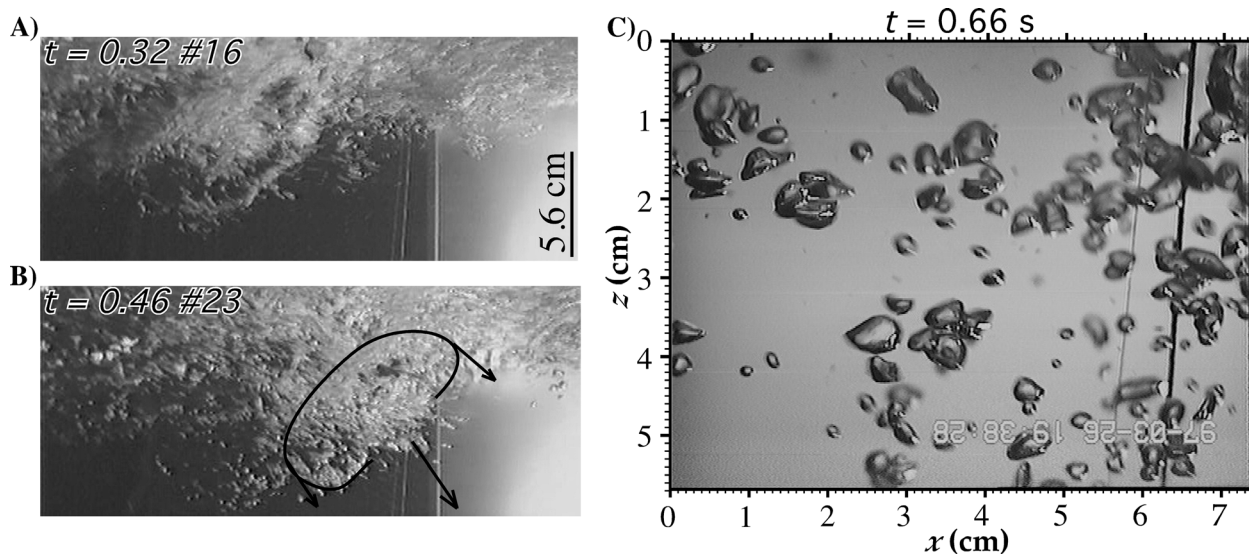


**Figure 14.** (a) Overview images of a BDe plume during early injection, (b) during mid-injection, and (c) at maximum penetration from wide FOV camera. Time  $t$ , horizontal (downwind) distance  $x$ , and depth  $z$ , with  $z = 0$  at 7.4 cm below average interface, are noted. Arrows in Figure 14b indicate motion of the bubble ring, which is also visible in Figure 14a. Figures 14a and 14b extend to  $\sim 15$  cm deep; size scale is shown in Figure 14a.

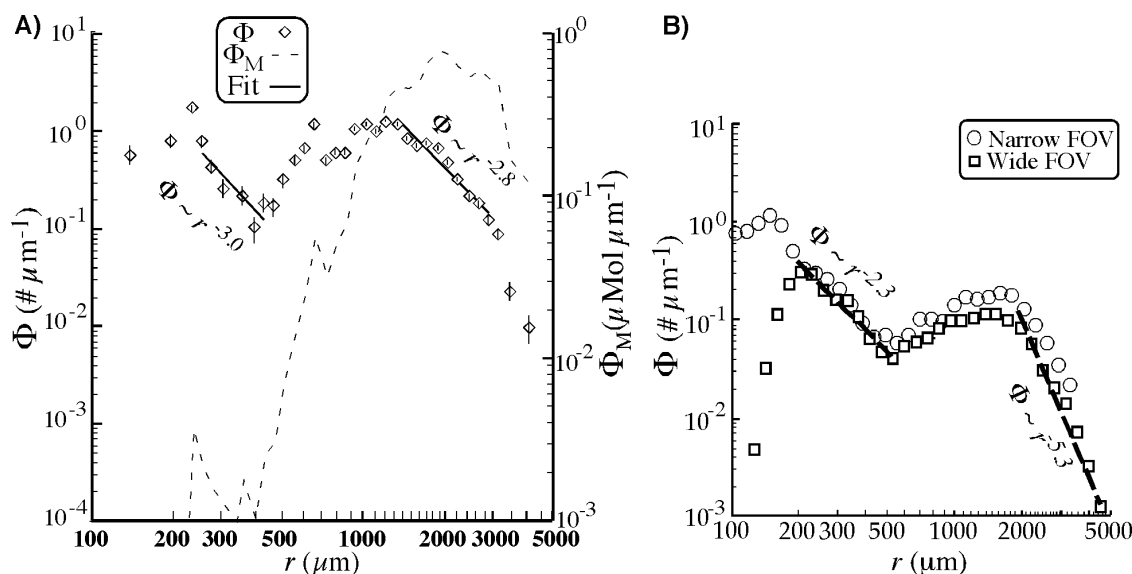


**Figure 15.** (a) Injection BDDe distribution  $\Phi$  and mass distribution  $\Phi_M$  versus radius  $r$  and fits to  $\Phi$ . (b) Average BDDe  $\Phi$  and  $\Phi_M$  versus  $r$  and fits to  $\Phi$ . Data key and  $r$  range of fit are shown in Figure 15a. Note that the scale for  $\Phi_M$  is greater than in all other figures. Error bars are  $\pm 1 \sigma$  (two plumes analyzed).

[52] The injection  $\Phi$  (Figure 15a) showed similar features to other dense plumes; large bubbles were more important in  $\Phi$  and  $\Phi_M$ , and it was clearly multimodal, with a well-resolved peak at  $r \sim 1500 \mu\text{m}$  and a possible, but inadequately resolved, peak at  $r \sim 600 \mu\text{m}$ . For bubbles with  $r > 1500 \mu\text{m}$ ,  $\Phi$  decreased with  $S = 2.8$ , then much more sharply with  $S = 7.8$  for  $r > 3000 \mu\text{m}$ . The small bubble  $\Phi$  also decreased steeply with  $S = 3.0$ , similar to other dense plumes. Lifetimes for BDDe plumes were the longest of all plume classes,  $\sim 1.5$  s and there were significant differences between the injection  $\Phi$  (Figure 15a) and the lifetime average  $\Phi$  (Figure 15b). Good agreement over a wide range of radii between the two cameras shows the lifetime-average plume was “well mixed” between these measurement volumes. The good agreement also shows that the difference in DOF and FOV between the two cameras was accounted for correctly by the scaling factors. The slight underestimate of the large bubble peak by the small camera may result from larger bubbles intersecting the edge of the narrow FOV camera’s image more frequently than smaller bubbles. Comparison of  $\Phi$  for the two cameras demonstrates that the decrease in  $\Phi$  for  $r < 200 \mu\text{m}$  for the wide FOV camera was from resolution limitations. In the lifetime-average  $\Phi$ , the large bubble peak was larger than for the injection  $\Phi$ ,  $\sim 1800 \mu\text{m}$ , with  $\Phi$  decreasing sharply for larger  $r$  ( $S = 5.3$ ).  $B_{VM}$  was significantly greater than other plume types,  $33 \text{ cm}^3$ , but since  $P_{VM}$  was  $\sim 10,000 \text{ cm}^3$ ,  $\varepsilon$  was  $\sim 0.33\%$ , that is, comparable to other deep dense plumes.

#### 4.5. Plume Heterogeneity and $\Phi$

[53] Shallow plumes showed significant heterogeneity with larger bubbles being injected more shallowly than smaller bubbles. Since these plumes were entirely in the FOV, this heterogeneity had no effect on  $\Phi$ . Deep, diffuse plumes exhibited strong depth dependency and were significantly larger than the FOV; thus, for them, the homogeneous assumption was poor. Fortunately these plumes

were quite rare and contributed little to overall bubble generation. For dense plumes, bubbles were distributed approximately homogeneously within the central plume region, and also within the peripheral region. However, a significant heterogeneity was that smaller bubbles largely were found in the plume periphery. For dense plumes there was no depth segregation for smaller bubbles, since they were found in both the deep and shallow peripheral plume regions. The central region could be further divided into upper and lower central regions depending on plume dynamics. For some plumes there was size segregation in which bubbles with  $r > 2500 \mu\text{m}$  primarily were injected into the upper central region. Bubbles also tended to begin rising in the upper central region earlier ( $\sim 0.1$  s) than the lower central plume. There was no obvious upper/lower central segregation for the largest dense plumes observed (BDDe and NDDe); that is, these plumes were well mixed.

## 5. Discussion

[54] Measured and calculated bubble plume class parameters are summarized in Table 3. Noninteraction class plumes (bold) were organized in Table 3 with regards to “formation energy,” using plume volume,  $P_{VM}$  (a proxy for generated fluid motions), or peak bubble volume,  $B_{VM}$  (a proxy for created surface area). The most significant observation was that two very distinct plume class types were observed, dense and diffuse, with very distinct  $\Phi$ , while there was great similarity in  $\Phi$  among diffuse plume classes or among dense plume classes. Specifically, diffuse plumes had a broad, shallow  $\Phi$  that decreased steeply for  $r > 1000 \mu\text{m}$ . In contrast, dense plumes were multimodal with the small bubble  $\Phi$  decreasing more steeply than for diffuse plumes and a peak at  $r \sim 1500\text{--}1800 \mu\text{m}$ . As a result, the large bubble population was significantly enhanced for dense plumes compared to diffuse plumes. Thus the background obscuration was due to these larger bubbles. In the

**Table 3.** Bubble Plume Class Parameters for Injection<sup>a</sup>

Class	$\tau$ , s	$z_p$ , cm	$\langle B_V \rangle$ , cm <sup>3</sup>	$\langle B_{VM} \rangle$ , cm <sup>3</sup>	$\langle P_{VM} \rangle$ , cm <sup>3</sup>	$\epsilon$ , %	$S_1$	$R$	$S_2$
Micro <sup>b</sup>	0.4	3.2	0.15	0.4	18	2.3	0.4	1000	2.5
NSDi <sup>b</sup>	0.7	6	0.44	0.8	120	0.66	1.0	1000	3.5
BSDi	0.6	6	0.88	1.8	300	0.63	—	—	—
BDDi	1.2	18	0.47	1.1	1200	0.09	2.6	1000	3.4
NDDi									
NSDe <sup>b</sup>	0.9	9	1.9	3.8	460	0.81	2.6	1700	3.0
BSDe	1.0	12	3.5	4.9	2400	0.20	2.6	1700	2.9
NDDe <sup>b</sup>	1.2	23	2.8	4.8	2400	0.20	2.0	1600	2.9
BDDe	1.5	33	5.2	33.	10,000	0.33	3.0	1500	2.8

<sup>a</sup>Here  $\tau$  is plume lifetime;  $z_p$  is maximum penetration depth;  $\langle B_V \rangle$  is average bubble volume during lifetime;  $\langle B_{VM} \rangle$  and  $\langle P_{VM} \rangle$  are bubble and plume volumes at maximum penetration, respectively;  $\epsilon$  is void fraction;  $S$  is power law exponent of bubble population; and  $R$  is critical radius where  $S$  changes.

<sup>b</sup>These are noninteraction classes.

following discussion, the interaction classes (BSDi, NDDi, BDDi, and BSDe) are neglected for reasons previously discussed.

### 5.1. Diffuse Plumes

[55] Most diffuse plumes analyzed were imaged in their entirety from formation to senescence. For small bubbles, the diffuse plume injection  $\Phi$  was very weakly dependent on  $r$ , with  $S$  varying between 0.6 (micro) and 1.1 (NSDi) from the small resolution size limit ( $r \sim 90$  and  $r \sim 200$   $\mu\text{m}$  for the narrow and wide FOV cameras, respectively) to  $r \sim 1000$   $\mu\text{m}$ . This shallow  $S$  during injection agrees with other observations that  $\Phi$  is significantly shallower closer to the formation region or time, than the background population, which is temporally and spatially averaged [e.g., Baldy and Bourgüel, 1987]. For comparison, for a seawater WST, Leifer [1995] reported at the earliest time accessible  $S = 2.4$ , similar to the WST values of Haines and Johnson [1995] for fresh and salt water,  $S = 2.6$  and  $S = 2.7$ , respectively. Deane and Stokes [2002] reported  $S = 1.8$  for an individual ocean bubble plume at an undetermined time after formation. These plumes exhibited some aspects of diffuse plumes (i.e., a critical radius, many small bubbles, but also some aspects of dense bubble plumes, such as the peripheral region with small bubbles [Haines and Johnson, 1995], and the presence of a large radius peak in the size distribution [Haines and Johnson, 1995; Deane and Stokes, 2002]). However, because Leifer [1995] and Haines and Johnson [1995] were for a WST, that is, different formation mechanism, it is unclear if the dense and diffuse classes are strictly appropriate. The greater small bubble population for bubble plumes in the ocean in Deane and Stokes [2002] than observed for dense bubble plumes in Luminy may be due to salinity or other factors.

[56] For diffuse plumes,  $S$  for small bubbles rapidly steepened with  $t$ . For example,  $S = -0.4$  (i.e.,  $\Phi \sim r^{+0.4}$ ) at maximum penetration ( $t = 0.22$  s) for the NSDi plume in Figure 5b, but by  $t = 0.26$  s,  $S$  had increased to 1.1. There are two possible causes of the increase in  $S(t)$  with  $t$ , the size dependency of the rise velocity,  $V_B$ , and size segregation during injection. For  $r < 700$   $\mu\text{m}$  at 20°C, the onset of oscillations [Leifer et al., 2000],  $V_B$  increases with  $r$  [Clift et al., 1978], thus both the bubble vertical flux and loss at the surface also increase with  $r$ . For larger bubbles,  $V_B$  decreases with  $r$  until  $r \sim 2200$   $\mu\text{m}$ , before gradually increasing again [Clift et al., 1978]. Thus the increase in  $S$

with  $t$  for the size range  $700 < r < 1000$   $\mu\text{m}$  (i.e., the critical radius) at the same rate as the increase in  $S$  with  $t$  for smaller ( $r < 700$   $\mu\text{m}$ ) bubbles cannot be explained by  $V_B(r)$ . This suggests the dominant cause was size segregation during injection; that is, larger bubbles were injected shallower. Such size segregation is readily visible in diffuse plume images (e.g., Figure 5a). Generally, small bubbles were injected faster and thus were preferentially located in the plume periphery. Thus one effect of size segregation is a steeper  $\Phi$  in the periphery (e.g., Figure 7). This peripheral/central plume size segregation agrees with Haines and Johnson [1995] where it was observed that  $S$  decreased with  $t$  as the plume arrived at 15 cm below the interface; that is, the main plume followed the peripheral plume at the camera depth. By 2.3 s after plume formation,  $S$  reached a minimum of 1.2.

### 5.2. Dense Plumes

[57] Dense bubble plumes mostly were produced at fetches where the wave field was well developed. They exhibited a greater  $B_{VM}$  and  $P_{VM}$  than diffuse plumes, indicating greater requisite formation energy. For example, although NSDi and NSDe plumes had similar dimensions, NSDe plumes persisted longer, presumably because of greater turbulence, and had higher  $B_{VM}$ . The most significant difference between dense and diffuse plumes was the presence of a large bubble peak at  $r \sim 1500$  to 1800  $\mu\text{m}$ , often with a minimum in  $\Phi$  at  $r \sim 1000$   $\mu\text{m}$ . For the radii range of the wide FOV camera, this large bubble peak was most important to both  $\Phi$  and  $\Phi_M$ , although when smaller bubbles are included (e.g., the narrow FOV camera, Figure 15b)  $\Phi$  favors small bubbles. In addition, for some dense plumes there was a poorly resolved peak at  $r \sim 600$ –700  $\mu\text{m}$  in the injection  $\Phi$  (Figure 15a versus Figure 15b). However, it is unclear from this data set if this peak is significant because of inadequate sample size to resolve the peak.

[58] Size segregation occurred in both dense and diffuse plumes. However, it appeared less uniform with size for dense plumes. For example, for dense plumes, bubbles larger than  $r \sim 500$   $\mu\text{m}$  generally were observed throughout the plume, while smaller bubbles primarily were observed in the plume periphery. In diffuse plumes, bubbles of all sizes showed evidence of size segregation. Observed bubble trajectories were initially jet-like (e.g., Figure 14) and thus plume injection probably was due to a descending jet of water. Small bubbles have lower drag [Clift et al., 1978],

lower buoyancy, and rise linearly in a static fluid [Leifer *et al.*, 2000]. Thus they are more easily injected by a descending jet. In contrast, larger bubbles have greater buoyancy, drag, and other forces, such as the lift force [Jakobsen *et al.*, 1997], thus they should be more difficult to inject. In addition, bubbles with  $r > 700 \mu\text{m}$  (the onset of oscillations), oscillate in a static fluid, which increases their drag [Clift *et al.*, 1978]. These larger bubbles may produce instabilities in the descending jet, decreasing the jet's ability to inject bubbles and hence their injection depth. In this conceptual model, instabilities in the jet do not develop first at the leading edge of the descending jet where the small bubbles are, but somewhat behind, where the larger bubbles are.

[59] In comparison with other reported  $\phi$ , the multimodal  $\Phi$  for dense plumes appears unique. However, when  $\Phi$  for dense and diffuse plumes were combined to calculate the global injection  $\Phi$ , the multimodal aspect was “hidden” (LCD), yielding a  $\Phi$  similar to a more common two-part  $\Phi$  such as Deane and Stokes [2002]. In particular, LCD showed a global  $\Phi$  with  $S = 1.2$  for  $r < 1700 \mu\text{m}$ , decreasing for larger  $r$  with  $S = 3.0$ . Close inspection of other published  $\phi$  suggests a similar multimodal  $\phi$ , albeit insufficiently resolved. For example, Haines and Johnson [1995] showed a peak in  $\phi$  at  $r \sim 3000 \mu\text{m}$  for fresh water. In the ocean, Deane and Stokes [2002] showed for one individual oceanic bubble plume at 30 cm depth a strong peak at  $r \sim 2500 \mu\text{m}$ , near their large size limit. From its high void fraction they interpreted it as being very young. However, two other plumes did not show a clear peak. The  $\phi$  of Baldy and Bourgu el [1987] above the trough also showed a second peak at  $2000 \mu\text{m}$  on the basis of laser measurements.

[60] Although BDe plumes were much less common than other dense plumes, about a tenth as frequent as NSDe plumes (LCD), their  $B_{VM}$  was roughly 10 times as great; thus their contribution to total injected bubbles or void fraction was comparable. However, because of their greater  $z_p$  and lifetime, bubble processes that are time- or depth-dependent, such as gas transfer, will be influenced more strongly by BDe plumes than other, shallower dense plumes (at least for LUMINY conditions).

### 5.3. Bubble Plume Formation and Energy

[61] Bubble plumes were observed with  $B_{VM}$  and  $P_{VM}$  spanning many orders of magnitude. However, void fractions spanned a much narrower range; less than an order of magnitude (neglecting interaction classes). When a wave breaks, energy is transformed into the formation of the bubbles (new surface area) and fluid motions (turbulence and bulk water motions). Bulk water motions from wave breaking include the injection jet, but not the upwelling flow from bubble buoyant rise (which is due to the injection of buoyant bubbles). Thus  $\epsilon$  at maximum penetration, when most of the injection energy has dissipated or been converted to potential energy and bubble distributions are still those of formation, represents a balance between conversion of wave-breaking energy to bubble formation and fluid motions including bubble injection. We consider the volume into which the bubbles were injected or dispersed a proxy for the breaking energy that went into fluid dynamics. Microplumes had the smallest  $B_{VM}$  and  $P_{VM}$  but the highest  $\epsilon$ , and were most important at the fetch of lowest wave development (LCD). In contrast, the largest dense plumes had the lowest  $\epsilon$

and were most important at the fetch of greatest wave development (LCD). We interpret this as a shift with increasing plume energy (i.e., wave-breaking energy) from bubble surface area formation toward fluid motion generation.

[62] Another important observation is that while diffuse plume classes and dense plume classes were observed, there were no plume classes with intermediate “optical density,” that is, no class that exhibited features of both dense and diffuse plumes. Thus the distribution of plume classes was bimodal, as was  $\Phi$  for dense plumes. This strongly suggests two different formation mechanisms or processes for dense and diffuse plumes, one that forms bubbles with  $r < 1000 \mu\text{m}$  that is weakly size-dependent, and a second mechanism that preferentially forms larger bubbles with a preferred size scale of  $r \sim 1700\text{--}2000 \mu\text{m}$ . The second peak in the dense plume  $\Phi$  is consistent with the bubble fragmentation mechanism of formation in which the plume begins as a single large void that fragments into large bubbles that themselves further fragment until surface tension prevents further fragmentation [Longuet-Higgins and Smith, 1983]. This mechanism is proposed to produce a “pile up” at a radius, apparently  $r \sim 1700\text{--}2000 \mu\text{m}$  in the case of LUMINY. However, energy considerations [Deane and Stokes, 2002; Gemrich and Farmer, 1999] suggest that the large bubble peak should occur at a larger size scale than  $2000 \mu\text{m}$  since for the highly forced waves in LUMINY there should be greater dissipation than in the ocean. Reasons for this discrepancy remain unclear. Also, the formation mechanism of the smaller distributions is uncertain.

[63] Because dense plumes require more energy to form (inferred from their dominance in the region of greatest wave breaking and greatest wave development), the bubble formation mechanism for  $r > 1700 \mu\text{m}$  must require more energy than the formation mechanism for diffuse plumes. This also implies that breaking waves with sufficient energy to form dense plumes are more likely to form dense plumes. Although it is likely that both mechanisms occur in the formation of dense plumes, the steeper, small bubble distribution observed for dense plumes suggests that when the two formation processes occur for one plume (as in dense plumes) the small bubble, diffuse plume mechanism is much less efficient (or less active) than the large bubble formation mechanism. This is further supported by the observation that the most characteristic “dense” plumes were the smallest (NSDe) and presumably because of their small size required the least energy to form. In such case, the diffuse plume formation mechanism seems to require a surplus of energy above what is required to form a dense plume. A more detailed discussion of bubble formation is beyond the scope of this paper.

### 5.4. Instantaneous Injection Assumption

[64] One other important observation regards the instantaneous injection assumption used in numerical bubble models [e.g., Woolf, 1993]. The observations presented show that for plume bubbles larger than  $r \sim 300\text{--}400 \mu\text{m}$  this assumption is poor since the injection and rise phases were of comparable time. It may be a reasonable assumption for small bubbles that enter the senescence phase, since  $V_B$  for small  $r$  is slow enough that the risetime to the surface can be much greater than the injection time. However, for small shallow bubbles [e.g., Baldy and Bourgu el, 1987] or NSDi and microplumes it is also inappropriate. On the basis of this conclusion, calcu-

lated bubble transfer rates for bubbles that do not equilibrate should be (to first approximation) double that predicted using the instantaneous injection assumption.

## 6. Conclusions

[65] Bubble plume bubble size distributions for nine different bubble plume classes were presented. Several classes resulted from plume-plume interactions causing increased lifetimes, but similar injection distributions. Other classes showed one of either two bubble population controlling aspects: They were either dense or diffuse, no intermediate classes were observed. Dense plumes exhibited a well-resolved large bubble peak at  $r \sim 1700$  to  $2000 \mu\text{m}$ , and were relatively poor in small bubbles, while diffuse plumes decreased very shallowly with  $r$  until  $r \sim 1000 \mu\text{m}$  after which they decreased steeply. These observations suggest that two different bubble plume bubble formation mechanisms occurred for wind stress induced wave breaking and were related to the bubble plume formation mechanism. It is unclear if the bubble plume and bubble formation processes that generated the wide range of bubble plumes observed for these wind stress induced breaking waves are directly analogous to other bubble plume and bubble formation mechanisms, such as tipping buckets or focused waves.

[66] Distributions steepened with time, which could only partially be explained by the relationship between rise velocity and size. Thus it was concluded that size segregation during injection also played a role. Given the different depths, lifetimes, and populations for the various classes, background populations will depend upon the formation rate of each plume class for the wave field considered. Finally, plume injection and rise phases were roughly comparable, thus for bubbles in the plume, the instantaneous injection assumption often used in numerical models leads to an underestimate of bubble lifetime and thus predicted rates for many plume bubble-mediated processes.

## Notation

$r$ , $\mu\text{m}$	equivalent spherical bubble radius.
$t$ , s	time.
$x$ , cm	horizontal position.
$z$ , cm	depth relative to mean interface.
$\phi$ , $\text{m}^{-3}$	bubble concentration size distribution.
$\Phi_{(r,f)}$ , $\mu\text{m}^{-3}$	bubble plume bubble population size distribution.
$S$	power law exponent.
$k$ , $\text{cm}^{-3} \mu\text{m}^{+S}$	constant.
$w$ , cm	plume horizontal extent.
$z_p$ , cm	plume penetration depth.
$\tau$ , s	plume lifetime.
$B_V$ , $\text{cm}^3$	volume of bubbles in the plume.
$B_{VM}$ , $\text{cm}^3$	maximum $B_V$ (at maximum penetration).
$\Phi_M$ , $\text{Mol} \mu\text{m}^{-1}$	bubble plume population bubble mass size distribution.
$\epsilon$ , %	void fraction.
$P_{VM}$ , $\text{cm}^3$	plume volume at maximum penetration.
$R$ , $\mu\text{m}$	critical radius in $\Phi$ .
$V_B$ , $\text{cm s}^{-1}$	rise velocity in stagnant water.

[67] **Acknowledgments.** Most of the work reported here was carried out as part of the LUMINY project, which was supported by the European

Commission EC DG XII, contract ENV4-CT95-0080, and TNO-FEL, with additional support from the Netherlands Ministry of Defense, assignment A95KM786. Part of the work of I. Leifer was carried out while he was employed by the National University of Ireland in Galway and when he was a visiting-scientist at TNO-FEL. The authors would like to thank IRPHE-IOA for the extensive laboratory support provided during LUMINY.

## References

- Baldy, S., and M. Bourgu el (1987), Bubbles between the wave trough and wave crest levels, *J. Geophys. Res.*, **92**(C3), 2919–2929.
- Blanchard, D. C. (1989), The ejection of drops from the sea and their enrichment with bacteria and other materials: A review, *Estuaries*, **12**(3), 127–137.
- Bowyer, P., and D. Woolf (2004), Gas exchange and bubble-induced supersaturation in a wind-wave tank, *J. Atmos. Oceanic Technol.*, **21**, 1925–1935.
- Caulliez, G. (2002), Statistics of geometric properties of breaking wind waves observed in the laboratory, in *Gas Transfer at Water Surfaces*, *Geophys. Monogr. Ser.*, vol. 127, edited by M. Donelan et al., pp. 31–37, AGU, Washington, D. C.
- Clift, R., J. R. Grace, and M. E. Weber (1978), *Bubbles, Drops, and Particles*, 380 pp., Elsevier, New York.
- Crawford, G. B., and D. M. Farmer (1987), On the spatial distribution of ocean bubbles, *J. Geophys. Res.*, **92**(C8), 8231–8243.
- Deane, G. B., and M. D. Stokes (2002), Scale dependence of bubble creation mechanisms in breaking waves, *Nature*, **418**, 839–843.
- De Leeuw, G., et al. (1999), Breaking waves and air-sea gas transfer (LUMINY), *Rep. FEL-99-C122*, edited by G. de Leeuw, TNO Phys. and Electron. Lab., The Hague, Netherlands.
- De Leeuw, G., et al. (2002), LUMINY: An overview, in *Gas Transfer at Water Surfaces*, *Geophys. Monogr. Ser.*, vol. 127, edited by M. Donelan et al., pp. 291–294, AGU, Washington, D. C.
- Gemmrich, J. R., and D. M. Farmer (1999), Observations of the scale and occurrence of breaking surface waves, *J. Phys. Oceanogr.*, **29**, 2595–2606.
- Graham, A., D. K. Woolf, and A. J. Hall (2004), Aeration due to breaking waves. part 1: Bubble populations, *J. Phys. Oceanogr.*, **34**, 989–1007.
- Haines, M. A., and B. D. Johnson (1995), Injected bubble populations in seawater and fresh water measured by a photographic method, *J. Geophys. Res.*, **100**(C4), 7057–7068.
- Jakobsen, H. A., B. H. Sannaes, S. Grevskott, and H. F. Svendsen (1997), Modeling of vertical bubble-driven flows, *Ind. Eng. Chem. Res.*, **36**, 4052–4074.
- Johnson, B. D., and R. C. Cooke (1979), Bubble populations and spectra in coastal waters: A photographic approach, *J. Geophys. Res.*, **84**(C7), 3761–3766.
- Leifer, I. S. (1995), A validation study of bubble mediated air-sea gas transfer modeling, Ph.D. thesis, Ga. Inst. of Technol., Atlanta.
- Leifer, I., and G. De Leeuw (2002), Bubble measurements in breaking-wave generated bubble plumes during the LUMINY wind-wave experiment, in *Gas Transfer at Water Surfaces*, *Geophys. Monogr. Ser.*, vol. 127, edited by M. Donelan et al., pp. 303–309, AGU, Washington, D. C.
- Leifer, I., and R. Patro (2002), The bubble mechanism for transport of methane from the shallow sea bed to the surface: A review and sensitivity study, *Cont. Shelf Res.*, **22**, 2409–2428.
- Leifer, I. S., R. K. Patro, and P. Bowyer (2000), A study on the temperature variation of rise velocity for large clean bubbles, *J. Atmos. Oceanic Technol.*, **17**(10), 1392–1402.
- Leifer, I., G. De Leeuw, and L. Cohen (2003a), Calibrating optical bubble size by the displaced mass method, *Chem. Eng. Sci.*, **58**, 5211–5216.
- Leifer, I., G. De Leeuw, and L. H. Cohen (2003b), Optical measurement of bubbles: System, design and application, *J. Atmos. Oceanic Technol.*, **20**(9), 1317–1332.
- Leifer, I., G. Caulliez, and G. de Leeuw (2006), Bubbles generated from wind-steepened breaking waves: 2. Bubble plumes, bubbles, and wave characteristics, *J. Geophys. Res.*, doi:10.1029/2004JC002676, in press.
- Liss, P. S., et al. (1997), Physical processes in the microlayer and the air-sea exchange of trace gases, in *The Sea Surface and Global Change*, edited by P. S. Liss and R. A. Duce, pp. 1–33, Cambridge Univ. Press, New York.
- Loewen, M. R., M. A. O’Dor, and M. G. Skafel (1996), Bubbles entrained by mechanically generated breaking waves, *J. Geophys. Res.*, **101**(C9), 20,759–20,770.
- Longuet-Higgins, M. S., and N. D. Smith (1983), Measurement of breaking by a surface jump meter, *J. Geophys. Res.*, **88**, 9823–9831.
- Medwin, H., and N. D. Breitz (1989), Ambient and transient bubble spectral densities in quiescent seas and under spilling breakers, *J. Geophys. Res.*, **94**(C9), 12,751–12,759.
- Monahan, E. C. (1986), The ocean as a source for atmospheric particles, in *The Role of Air-Sea Exchange in Geochemical Cycling*, edited by P. Buat-Menard, pp. 129–163, Springer, New York.
- Patro, R. K., I. Leifer, and P. Bowyer (2002), Better bubble process modeling: Improved bubble hydrodynamics parameterization, in *Gas*

- Transfer and Water Surfaces, Geophys. Monogr. Ser.*, vol. 127, edited by M. Donelan et al., pp. 315–320, AGU, Washington, D. C.
- Stokes, D., G. Deane, S. Vagle, and D. Farmer (2002), Measurement of large bubbles in open ocean whitecaps, in *Gas Transfer at Water Surfaces, Geophys. Monogr. Ser.*, vol. 127, edited by M. Donelan et al., pp. 279–284, AGU, Washington, D. C.
- Thorpe, S. A. (1982), On the clouds of bubbles formed by breaking wind-waves in deep water and their role in air-sea gas transfer, *Philos. Trans. R. Soc. London, Ser. A*, 304, 155–210.
- Thorpe, S. A. (1986), Bubble clouds: A review of their detection by sonar, of related modes, and of how  $K_v$  may be determined, in *Oceanic Whitecaps*, edited by E. C. Monahan and G. Mac Niocaill, pp. 57–68, Springer, New York.
- Woolf, D. K. (1993), Bubbles and the air-sea transfer velocity of gases, *Atmos. Ocean*, 31(4), 517–540.
- Wu, J. (1979), Oceanic whitecaps and sea state, *J. Phys. Oceanogr.*, 9, 1064–1068.
- 
- G. de Leeuw, TNO Physics and Electronics Laboratory, P.O. Box 96864, NL-2509 JG, The Hague, Netherlands. (deleeuw@fel.tno.nl)
- I. Leifer, Marine Science Institute, University of California, Santa Barbara, CA 93106-5080, USA. (ira.leifer@bubbleology.com)